ELSEVIER

Journal of Structural Geology 28 (2006) 621–640

JOURNAL OF STRUCTURAL GEOLOGY

www.elsevier.com/locate/jsg

Mechanisms of weak phase interconnection and the effects of phase strength contrast on fabric development

Caleb W. Holyoke III *, Jan Tullis

Department of Geological Sciences, Brown University, Providence, RI 02912, USA

Received 25 April 2005; received in revised form 24 January 2006; accepted 30 January 2006
Available online 15 March 2006

Abstract

To determine how deformation mechanisms and fabrics evolve during the strain weakening and localization that accompany the transition from a load-bearing framework to an interconnected weak phase, shear experiments were conducted on a fine-grained gneiss (58% quartz, interconnected; 28% plagioclase, dispersed; 13% biotite, aligned but dispersed) at 745 and 800 °C, 1500 MPa and two strain rates (2×10^{-5} and 2×10^{-6} s^{-1}). In experiments with a high phase strength contrast (HPSC, 25× and 45×) between dispersed biotite and framework quartz grains, biotite grains become interconnected due to stress concentration at their tips that allow local semi-brittle flow of intervening quartz and cataclasis of intervening plagioclase. In the higher temperature HPSC samples, the biotite partially dehydrated in high strain zones; a single narrow shear zone formed because the PSC between the quartz and biotite/reaction product layers remained high. In the lower temperature HPSC samples there was no reaction, and a penetrative S–C′ fabric formed. The fabric is defined by the many multiply interconnected biotite strands that formed because the PSC between the quartz and biotite decreased as the biotites kinked. In slower strain rate experiments with a much lower PSC (~10×), biotite interconnection occurs by shearing into quartz/quartz boundaries where new, weak strain-free recrystallized grains form. At low strain a weak S–C′ fabric forms, but it evolves to an S–C fabric as the PSC decreases with strain. Thus, the magnitude of the strength contrast between a weak phase and its matrix influences the mechanism of weak phase interconnection, the degree of strain localization and the fabric.

Keywords: Strain localization; Load bearing framework; Phase strength contrast; Weak phase interconnection; Shear zone; Phase fabric

1. Introduction

Ductile shear zones occur on all scales in the crust and require a strain weakening process for their initiation. The processes that occur after strain localization can be deduced from the preserved microstructures, but microstructural evidence of the processes responsible for the initial weakening and localization is obliterated by subsequent strain. Possible strain weakening processes have been summarized by Poirier (1980) and White et al. (1980); some of these apply to monophase aggregates, but in the case of polyphase aggregates one of the most important is likely to be the interconnection of an initially dispersed weak phase (e.g. Handy, 1990; Stewart et al., 2000; Imber et al., 2001). Handy (1990, 1994) has emphasized the importance of the transition from a load-bearing framework (LBF) to an interconnected weak phase (IWP), but the specific processes by which polyphase aggregates accomplish such a transition are not well understood, nor are the conditions under which such a transition does or does not lead to a localized shear zone.

Several previous experimental studies have been performed on polyphase rocks or rock analogs to document the weakening associated with a change from a LBF to an IWP, including halite–calcite (Jordan, 1987), mica–quartz/feldspar (Gottschalk et al., 1990; Shea and Kronenberg, 1992, 1993; Tullis and Wenk, 1994; Rawling et al., 2002), quartz–feldspar (Dell'Angelo and Tullis, 1996), camphor–octachloropropane (Bons and Cox, 1994), and muscovite/kaolinite–halite (Bos and Spiers, 2001, 2002; Neimeijer and Spiers, 2005). In low temperature axial compression experiments on mica-bearing aggregates, Gottschalk et al. (1990), Shea and Kronenberg (1992, 1993) and Rawling et al. (2002) observed that stress concentrations at the tips of mica grains caused an increased density of microfracturing in adjacent quartz and feldspar grains, allowing brittle failure of the quartz/feldspar framework and interconnection of the micas. However, these studies were performed at conditions where monophase aggregates of the matrix quartz and feldspar are brittle, and a number of questions remain. What grain-scale deformation mechanisms

* Corresponding author. Tel.: +1 401 863 1923; fax: +1 401 863 2058.
E-mail address: Caleb_Holyoke_III@brown.edu (C.W. Holyoke).

0191-8141/$ - see front matter © 2006 Elsevier Ltd. All rights reserved.
doi:10.1016/j.jsg.2006.01.008

allow interconnection of weak phases such as micas at conditions where the framework minerals undergo ductile deformation? How are the mechanisms that cause ductile strain localization affected by the strength contrast between the weak phase and the framework? Does the phase strength contrast affect the degree of strain localization and/or the formation of an S–C or an S–C′ fabric? How do the fabrics respond to changes in the strength contrast or deformation mechanisms during deformation? An experimental study of a fine-grained gneiss was designed to answer these questions by allowing direct observation of several stages in the evolution of deformation mechanisms and fabrics during the transition from a load-bearing framework (quartz/plagioclase) to an interconnected weak phase (biotite) at three sets of conditions where the framework phases deform ductilely and there are a wide range of initial differences in strength between the framework and the weak phase (45×, 25×, and 10×).

2. Experimental procedures

Our goal was to understand the evolution of the deformation behavior and properties of a common polyphase aggregate, a fine-grained biotite + plagioclase + quartz gneiss, in terms of the properties of its constituent phases. We deformed the gneiss in general shear in a Griggs-type rock deformation apparatus (e.g. Tullis and Tullis 1986) at three sets of conditions; for comparison we sheared monophase aggregates of quartz and plagioclase at the same conditions, and we did two axial compression experiments on synthetic biotite aggregates. Experimental conditions were chosen to produce a range in the strength ratio between the stronger framework quartz–plagioclase and the weaker and initially dispersed biotite. We will use the term phase strength contrast (PSC) to describe that difference in strength. The initial PSCs for the three sets of experimental conditions were determined from the peak strengths of monophase aggregates deformed at the same temperature and bulk shear strain rate, and are used to interpret the yield behavior of the gneiss samples. Changes in the PSC after moderate to high strain were estimated from microstructural comparisons with other monophase aggregates.

2.1. Starting materials

Ten experiments were conducted using the Gneiss Minuti (Zurbriggen et al., 1998), a fine-grained (~150 ± 25 μm) gneiss consisting of muscovite + biotite + plagioclase + quartz ± minor garnet/monazite/Fe–Ti oxides (Table 1). The rock has layers of varied composition, but all samples were cored from two layers of the gneiss composed of 13% biotite, 28% plagioclase ($An_{27.7}$-$Ab_{71.9}Or_{0.4}$), 58% quartz and 1% garnet/Fe–Ti oxides (Fig. 1a). Quartz and plagioclase grains are relatively equant and have no optically visible deformation microstructures. The biotite grains are moderately well aligned, but not interconnected. Quartz grains form an interconnected framework and plagioclase grains are relatively isolated within it.

For the monophase aggregate experiments we used Black Hills quartzite (Fig. 1b, d ~ 100 μm), Tanco albite (Fig. 1c, d ~ 150 μm), and hot-pressed biotite aggregates. The Black Hills quartzite is composed of 99% quartz and 1% iron oxides/clay minerals/feldspar and contains no deformation features. The Tanco albite is 98% albite and 2% Al_2SiO_5 and has a moderate foliation. Fine-grained (~60 μm) aggregates of biotite were produced by hot-pressing biotite powders (Standard 2 Biotite of Fortier and Giletti (1991)) at 800 °C and a confining pressure (P_c) of 1500 MPa for 16 h prior to deformation. The weight percents of Fe and Mg in the Standard 2 Biotite are similar to those of the biotite in the Gneiss Minuti starting material, although the Standard 2 Biotite is less aluminous (Table 2). In the biotite-only aggregate samples most (001) became aligned perpendicular to σ_1 during hot-pressing, which maximized the peak strength. To estimate a lower bound for biotite strength, we used the flow law for slip on (001) of Kronenberg et al. (1990), calculated for the conditions of our experiments. These strengths are 33 and 29 MPa, below the stress resolution when using an all-salt assembly in the Griggs apparatus (~50 MPa; Post and Tullis, 1999).

2.2. Experimental conditions

Three sets of experiments were performed at $P_c = 1500$ MPa with no added water to produce a range of PSCs between the individual phases of the Gneiss Minuti (Table 1). The experimental conditions will be referred to by their temperature and F for fast (2×10^{-5} s^{-1}) or S for slow (2×10^{-6} s^{-1}) shear strain rate (e.g. 745S, 800F, and 800S). The experimental conditions were chosen to avoid biotite dehydration; however, minor amounts of reaction did occur after the initial interconnection of the weak phase, for all sets of conditions. Deformed samples of Standard 2 Biotite contain no reaction products, but its low Al content compared with that in the Gneiss Minuti may affect the breakdown temperature (Table 2). Separate Gneiss Minuti experiments were performed at the 800S conditions with 0.18 wt% water added, but this did not prevent biotite breakdown (Holyoke, 2005). Additional hydrostatic experiments using both cores and powders (2–75 μm) of the Gneiss Minuti were performed at $P_c = 1500$ (750 and 800 °C) and 2000 MPa (800 °C only) for ~90 h. Only a trace (~1%) of reaction products was observed in the 800 °C cores (both 1500 and 2000 MPa) and no reaction products were observed in the 750 °C core. More reaction products were observed in powders than in cores in all experiments. The most reaction was observed in the powdered half of the sample held at 800 °C/2000 MPa (~4% by volume), about 1% by volume was observed in the powdered half of the 800 °C/1500 MPa sample, and <1% was observed in the powdered half of the sample from the 750 °C/1500 MPa experiment. These results, described in more detail in Holyoke and Tullis (submitted), indicate that the biotite is no longer stable at higher pressures (and presumably at higher mean stresses) and higher temperatures. No melt was observed in any sample from this study.

Two sets of HPSC experiments were done at two different strain rate/temperature combinations; one set had almost no

Table 1
List of experiments

Experiment set	Experiment	Material	Temperature (°C)	Pressure (MPa)	Strain rate (1/s)	Total shear strain	Percent thinning	Phase fabric	Yield strength (MPa)[a]	Minimum strength after yield (MPa)[b]	Initial PSC
745S	W-1173	Gneiss Minuti	745	1500	2×10^{-6}	1	10	None	1340 (0.6)	Same	25×
	W-1137	Gneiss Minuti	745	1500	2×10^{-6}	1.6	10	Weak S–C′	1190 (0.7)	830	25×
	W-1139	Gneiss Minuti	745	1500	2×10^{-6}	3.1	34	S–C′	1300 (0.5)	640	25×
	W-1156	Gneiss Minuti	745	1500	2×10^{-6}	4	33	S–C′	1240 (0.5)	730	25×
	W-1153	Black Hills quartzite	745	1500	2×10^{-6}	2.9	24	S–C′	770 (0.8)	400	NA
	W-1176	Tanco albite	725	1500	2×10^{-6}	0.5	9	S–C′	1300 (0.4)	1130	NA
800F	W-1019	Gneiss Minuti	800	1500	2×10^{-5}	0.6	10	None	1330 (0.6)	1320	45×
	W-1009	Gneiss Minuti	800	1500	2×10^{-5}	1.1	17	Weak S–C′	1300 (0.5)	920	45×
	W-1008	Gneiss Minuti	800	1500	2×10^{-5}	3.3	37	Single shear zone	1280 (0.4)	510 (2.6)	45×
	W-1093	Black Hills quartzite	800	1500	2×10^{-5}	2.3	8	S–C′	1390 (2.3)	Same	NA
	W-1105	Black Hills quartzite	800	1500	2×10^{-5}	6.1	43	S–C′	1350 (1.6)	910	NA
	W-1202	Biotite Standard 2	800	1500	2×10^{-5}	50%[c]	NA	None	340 (14%)	110	NA
	W-1117	Tanco albite	800	1500	2×10^{-5}	0.5	8	S–C′	1430 (0.1)	1150 (0.5)	NA
800S	W-1076	Gneiss Minuti	800	1500	2×10^{-6}	0.6	11	Proto-S–C′	650 (0.4)	620	10×
	W-1079	Gneiss Minuti	800	1500	2×10^{-6}	1.5	17	S–C′	520 (0.5)	230	10×
	W-1020	Gneiss Minuti	800	1500	2×10^{-6}	5.4	45	S–C	500 (0.6)	200 (2.5)	10×
	W-1106	Black Hills quartzite	800	1500	2×10^{-6}	3.7	38	S–C	290 (0.4)	160	NA
	W-1199	Biotite Standard 2	800	1500	2×10^{-6}	48%[c]	NA	None	90 (32%)	60	NA
	W-1112	Tanco albite	800	1500	2×10^{-6}	4.2	30	S–C′	1740 (4.2)	Same	NA

[a] Shear strain of yield in parentheses.
[b] Shear strain of minimum strength after yield in parentheses if not equal to total shear strain.
[c] Axial compression experiment.

biotite reaction and the other had significant reaction in high strain regions. At the lower temperature/slower strain rate conditions (745S) four experiments on the Gneiss Minuti were performed to shear strains (γ) of 1 (at yield), 1.6 (during weakening), and 3.1 and 4 (after deformation at an approximately constant stress was achieved, hereafter referred to as mechanical steady state), with associated thinning of the sample perpendicular to the shear plane of 10, 10, 34, and 33%, respectively. One experiment was performed on Black Hills quartzite at the same conditions to $\gamma=2.9$, with associated thinning of 24%. At the higher temperature/faster strain rate conditions (800F) three experiments on the Gneiss Minuti were performed to $\gamma=0.6$ (at yield), $\gamma=1.1$ (during strain weakening), and $\gamma=3.3$ (after mechanical steady state flow was achieved), with associated thinning of 10, 17, and 34%, respectively. At the same conditions, comparison experiments were done on Black Hills quartzite ($\gamma=2.3$ and 6.1) and on Tanco albite ($\gamma=0.5$), with 8, 43, and 8% thinning. An axial compression experiment was performed on Standard 2 Biotite powders ($\sim$60 μm) at the same conditions to 50% shortening to determine the maximum strength of biotite.

A single set of LPSC experiments was performed at 800S. Three samples of the Gneiss Minuti were deformed to $\gamma=0.6$ (at yield), $\gamma=1.1$ (during weakening), and $\gamma=5.2$ (after mechanical steady state flow was achieved), with associated thinning of 11, 17, and 45%, respectively. Comparison experiments were done on Black Hills quartzite ($\gamma=3.6$) and Tanco albite ($\gamma=4.4$) with thinning of 38 and 30%, respectively

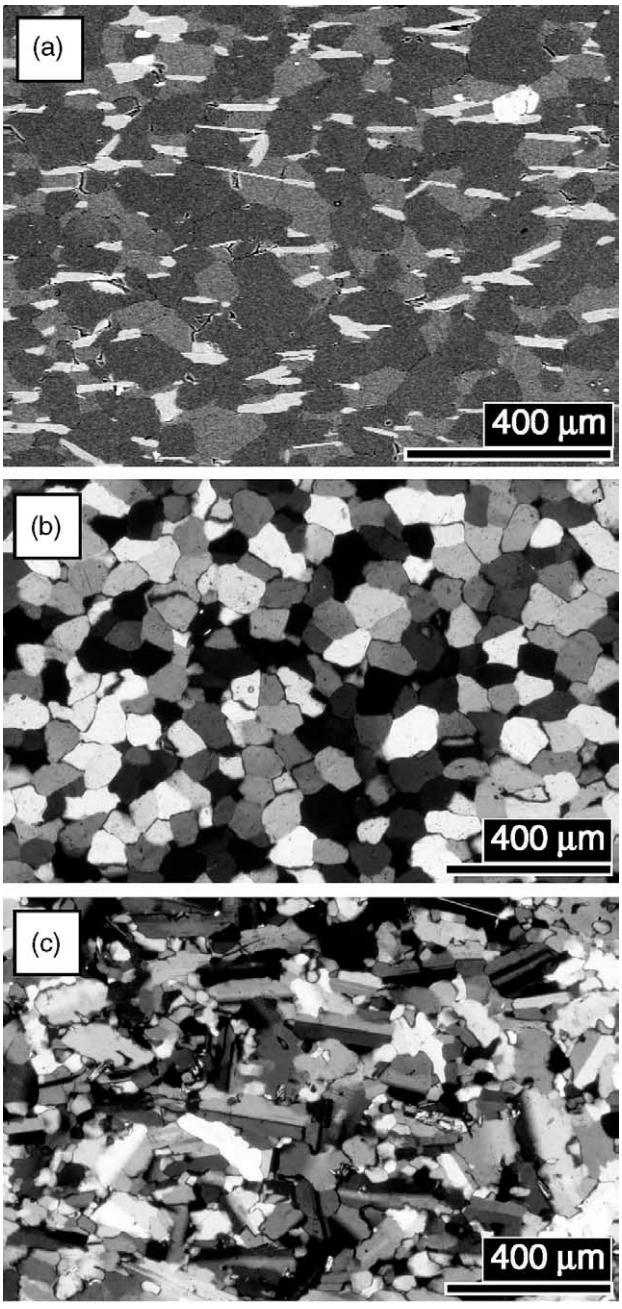

Fig. 1. Photomicrographs of starting materials. (a) Gneiss Minuti, SEM-BSE (back scattered electron) micrograph. ~100–150 μm grain size, 55% quartz (darkest grey grains), 33% plagioclase (An_{30}—intermediate grey grains), 12% biotite (white grains). The biotite grains are aligned but not interconnected; quartz grains form an interconnected framework. (b) Black Hills quartzite, crossed nicols; ~100 μm grain size. (c) Tanco albite, 50–200 μm grain size, 98% plagioclase (An_1), ~2% Al_2SiO_5, foliation horizontal.

(Table 1). An axial compression experiment using Standard 2 Biotite was performed at the same conditions to 48% shortening to determine the maximum strength of biotite.

2.3. Experimental methods

For the Gneiss Minuti samples, 6.35 mm diameter cores were made with the foliation oriented at 45° to the core length.

Table 2
Average weight percent oxide compositions of biotite in Gneiss Minuti and Standard 2 Biotite starting materials

Oxide	GM average (wt% ox)	BS2 (wt% ox)[a]
SiO_2	35.6	36.6
Al_2O_3	19.5	17.2
FeO	20.6	20.0
MgO	9.2	9.7
CaO	0.1	0.2
Na_2O	0.1	0.3
TiO_2	2.3	3.2
MnO	0.2	0.3
Cr_2O_3	0.0	NM
K_2O	8.6	8.7
F	0.2	NM
Total	96.4	96.2

NM—not measured.
[a] From Fortier and Giletti (1991).

Slices ~1.27 mm thick were cut from these cores parallel to the foliation, and placed between two 45° cut Al_2O_3 pistons, which had shallow grooves cut into the shearing surfaces normal to the shear direction to grip the samples (Fig. 2). The shear assembly was inserted in an inner Pt jacket with Pt and Ni discs at each end, and an outer Cu jacket (Fig. 2). Samples were kept in an oven at 90 °C for at least 24 h prior to installing them in the solid-NaCl assembly (Fig. 2).

Samples were taken to run conditions (T=745/800 °C, P_c=1500 MPa) over a period of ~4–5 h. Upon reaching run conditions for fast strain rate experiments, the motor was turned on at a constant displacement rate of 6.6×10^{-3} cm/h and the top piston 'hit' the sample approximately 8–12 h later. For the slow strain rate experiments the displacement rate was 6.6×10^{-4} cm/h, and it took 3–5 days to 'hit' the sample. After the desired shear strain was achieved the temperature was quenched rapidly to 300 °C; then the samples were slowly (over 1–2 h) brought to room temperature and pressure to minimize decompression cracking.

Deformed samples were impregnated with epoxy for thin section preparation. Doubly polished thin sections oriented parallel to the XZ plane were prepared for standard petrographic analysis and scanning electron microscopy (SEM); separate sections were made for transmission electron microscopy (TEM). Force–displacement data were corrected for decreasing area of overlap of the 45° cut pistons, for thinning of the sample, and for friction within the assembly in order to produce plots of differential stress vs. shear strain (see Heilbronner and Tullis (2002, submitted) for details of the data correction methods). The estimated errors for stress measurement using the all-salt assembly are ±50 MPa (Post and Tullis, 1999). Therefore, the stresses have been rounded off to the nearest 10 MPa.

3. Results

3.1. Mechanical data

The stress–strain curves for all three sets of the Gneiss Minuti samples (Fig. 3b, d and f) show pronounced strain

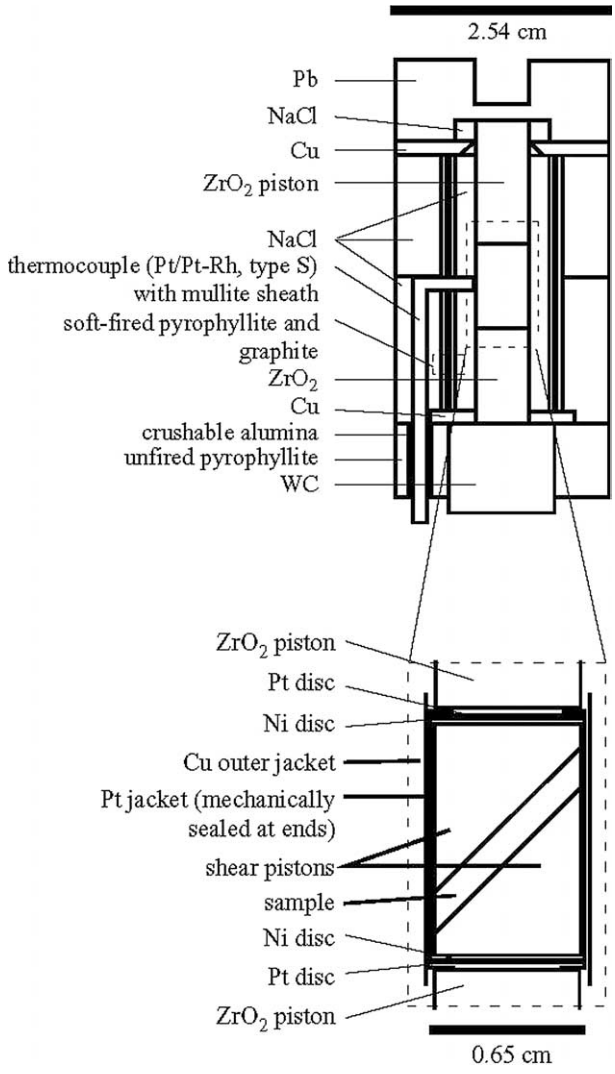

Fig. 2. All-NaCl sample assembly used in experiments. The grooves on the shear pistons used to grip samples are not shown. The samples used for axial compression experiments on hot-pressed biotite aggregates have the same volume as the shear piston/sample slice presented above.

weakening. At HPSC conditions (800F and 745S) the Gneiss Minuti samples have a peak strength ~200 MPa lower than the confining pressure followed by weakening to between 45 and 60% of the peak strength by a shear strain of about 2.5 (Fig. 3b and d). The slight hardening at $\gamma > 3$ is due to the faster strain rate resulting from sample thinning. The Black Hills quartzite samples deformed at 800 °C, $\dot{\gamma} = 2 \times 10^{-5}\ s^{-1}$ (800F) were stronger than the Gneiss Minuti samples, whereas the Tanco albite sample had approximately the same peak strength (Fig. 3a). However, the Black Hills quartzite sample deformed at 745 °C, $\dot{\gamma} = 2 \times 10^{-6}\ s^{-1}$ (745S) was weaker than the Gneiss Minuti samples deformed at the same conditions (Fig. 3c). The Standard 2 Biotite sample deformed at 800F in axial compression had a peak strength of 340 MPa ($\varepsilon = 14\%$) prior to strain weakening to 110 MPa at the end of the experiment ($\varepsilon = 50\%$) (Fig. 3a).

At LPSC conditions (800S) the peak strength of the Gneiss Minuti samples was much lower than that at the HPSC conditions (~560 MPa), but these samples also weakened to about half the peak strength by $\gamma = 1.5$ (Fig. 3f), similar to the HPSC samples. At this strain rate the Black Hills quartzite sample had a lower peak strength than the Gneiss Minuti samples, although its steady state flow strength was about the same as that of the high strain, weakened Gneiss Minuti samples (Fig. 3e). The peak strength of the Tanco albite samples was much higher than those of the Gneiss Minuti or Black Hills quartzite samples and was followed by strain hardening (Fig. 3e). The Standard 2 Biotite sample deformed in axial compression at 800S had a peak strength of 90 MPa ($\varepsilon = 12\%$) and strain weakened to a steady state flow stress of ~60 MPa ($\varepsilon = 48\%$) (Fig. 3e). The strengths of all Black Hills quartzite and Tanco albite samples from experiments performed at 745S, 800F, and 800S conditions are consistent with previous experimental studies in which these materials were deformed in axial compression (Hirth and Tullis, 1992, 1994; Post and Tullis, 1999).

3.2. Microstructures

3.2.1. Introduction

Microstructural observations of each sample at optical, SEM and TEM scales are presented in four separate sections: monophase and polyphase aggregates (Sections 3.2.2.1 and 3.2.2.2, respectively) deformed at $T/\dot{\gamma}$ conditions producing a HPSC in the Gneiss Minuti samples (745S and 800F), and monophase and polyphase aggregates (Sections 3.2.3.1 and 3.2.3.2, respectively) deformed at $T/\dot{\gamma}$ conditions producing a LPSC in the Gneiss Minuti samples (800S). Because quartz forms the interconnected framework in the Gneiss Minuti and its deformation mechanisms and the microstructures they produce are more sensitive to stress and strain rate variations at the experimental conditions of this study than those of biotite and plagioclase, quartz microstructures are described in more detail than those of plagioclase and biotite. Changes in quartz microstructures are used to infer changes in deformation processes that accompany strain localization. Therefore, we will first briefly review the microstructures produced by different deformation mechanisms in quartz that apply to this study, prior to describing our results. These microstructures are described in detail by Hirth and Tullis (1992, 1994).

The deformation mechanisms operating in quartz aggregates and the microstructures produced by these mechanisms are stress-dependent. (1) At high stresses, approaching or exceeding the confining pressure, a combination of dislocation glide and brittle microcracking occurs. Optical-scale microstructures produced by semi-brittle flow include patchy undulatory extinction, cracks in porphyroclasts and minor bulging recrystallization at grain boundaries. The cracking is mainly at the grain-scale; through-going faults do not develop. TEM-scale microstructures include high densities of tangled and/or straight dislocations as well as microcracks in porphyroclasts and a few strain-free recrystallized grains (< 1 μm) at their edges. (2) At stresses below the confining pressure cracks do not open; strain is accomplished by dislocation glide and recovery occurs by bulging

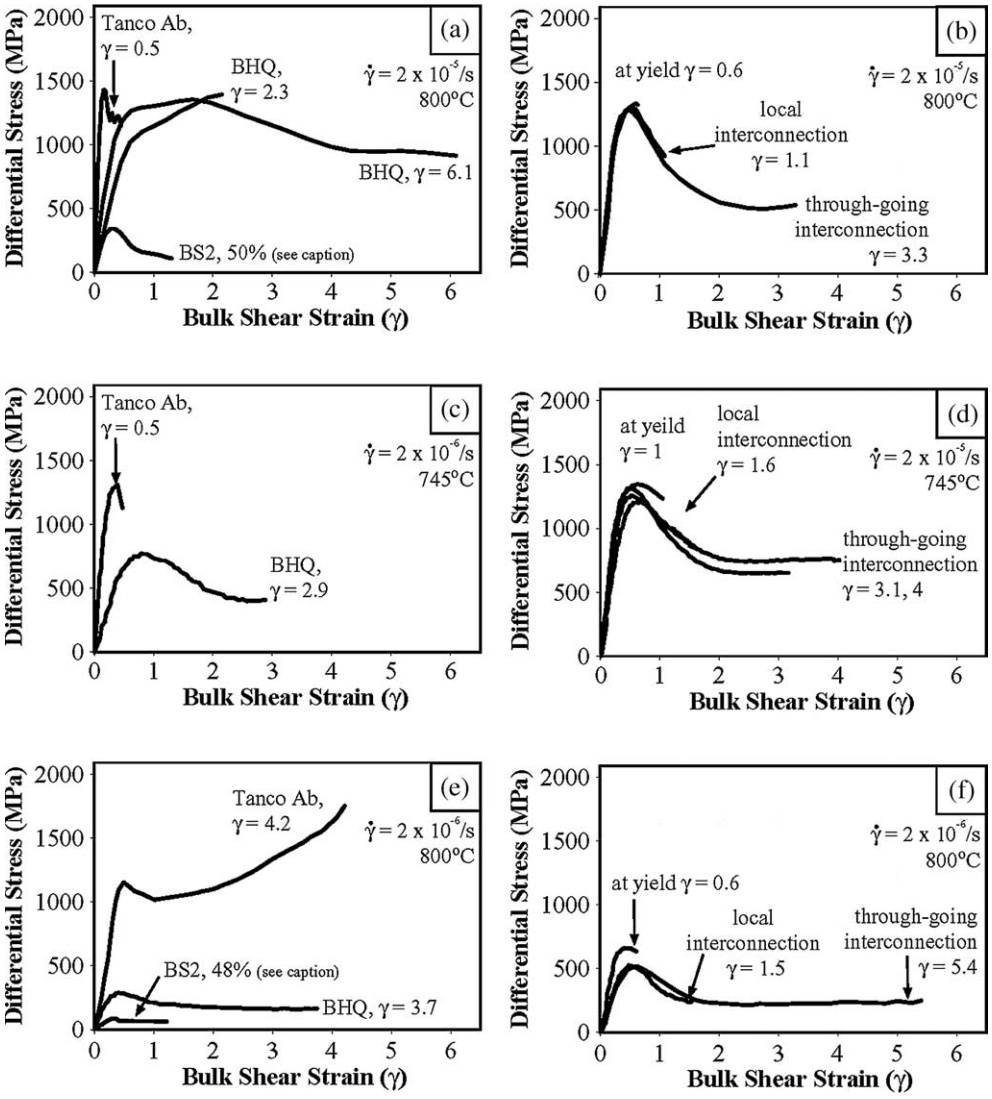

Fig. 3. Differential stress vs. bulk shear strain plots for Black Hills quartzite (BHQ), Tanco albite (Tanco Ab), Standard 2 Biotite (BS2) (a) and Gneiss Minuti (b) experiments conducted at $T = 800$ °C, $P_c = 1500$ MPa, $\dot{\gamma} = 2 \times 10^{-5}$ s^{-1}, and Black Hills quartzite/Tanco albite (c) and Gneiss Minuti (d) experiments conducted at $T = 745$ °C, $P_c = 1500$ MPa, $\dot{\gamma} = 2 \times 10^{-6}$ s^{-1}, and Black Hills quartzite, Tanco albite, Standard 2 Biotite, (e) and Gneiss Minuti (f) experiments conducted at $T = 800$ °C, $P_c = 1500$ MPa, $\dot{\gamma} = 2 \times 10^{-6}$ s^{-1}. Standard 2 Biotite strain values were converted from percent strain to strain magnitude and then to shear strain to compare them with the general shear geometry samples according to the methods described in Heilbronner and Tullis (2002). The flow law of Kronenberg et al. (1990) for slip on (001)[100] predicts that the flow stresses for biotite at $\dot{\gamma} = 2 \times 10^{-5}$ s^{-1} and $\dot{\gamma} = 2 \times 10^{-6}$ s^{-1} are 33 and 29 MPa, respectively.

recrystallization. The optical-scale microstructures produced by recrystallization-accommodated dislocation creep include patchy undulatory extinction, deformation lamellae and minor elongation in porphyroclasts and mantles of very small recrystallized grains at their edges. TEM-scale microstructures include high densities of tangled dislocations in porphyroclasts and finely sutured grain boundaries with zones of small (1–2 μm) recrystallized grains. (3) At stresses <300 MPa recovery occurs dominantly by dislocation climb and some grain boundary migration. The optical-scale microstructures produced by climb-accommodated dislocation creep include elongate ('ribbon') porphyroclasts with patchy zones formed by subgrains and zones of fine recrystallized grains (>2–4 μm) at their edges. The TEM-scale microstructures include dislocation walls, subgrains and low densities of curved dislocations in porphyroclasts and recrystallized grains produced by a combination of subgrain rotation and grain boundary migration. Microstructures formed at even lower flow stresses are described by Hirth and Tullis (1992) and Stipp et al. (2002a,b); however, none of these microstructures were observed in any of the samples in this study. Feldspars develop a similar sequence of microstructures (e.g. Tullis, 2002), but they occur at higher temperatures than those observed in quartz.

Two types of strain fabrics, originally described from naturally deformed rocks, developed in the samples: S–C′ and S–C. In rocks with a right lateral sense of shear, these fabrics are defined by the orientation of the foliation plane (S) and the shear planes (C and C′), which are oriented at 45° counter-clockwise and 0 and ~20° clockwise from the shear plane, respectively. In our samples the foliation plane is defined by the long axes of porphyroclasts of quartz, plagioclase, and

biotite. The shear planes are defined by zones of recrystallized quartz or plagioclase and/or highly sheared biotite grains, which are sometimes mixed with fine-grained reaction products. These fabrics are illustrated schematically in Fig. 12 and described in Passchier and Trouw (1995).

3.2.2. High phase strength contrast experiments

3.2.2.1. Monophase aggregates. Three experiments were conducted using Black Hills quartzite at both sets of HPSC conditions, two at 800F and one at 745S, to determine the peak strengths and the microstructures at peak strength (low strain) and at high strain. The 800F sample (W1093) deformed to $\gamma = 2.3$ was very strong (1390 MPa). Deformation in the sample is homogeneous; deformation bands and lamellae are present in many porphyroclasts and very small recrystallized grains ($\sim$10 vol.%) occur along porphyroclast boundaries (Fig. 4a). TEM shows that most porphyroclasts have high densities of tangled dislocations and strain-free recrystallized grains at their margins (Fig. 4b). A few porphyroclasts were observed to have straight dislocations with nearly perpendicular microcracks (Fig. 4c). These microstructures are characteristic of

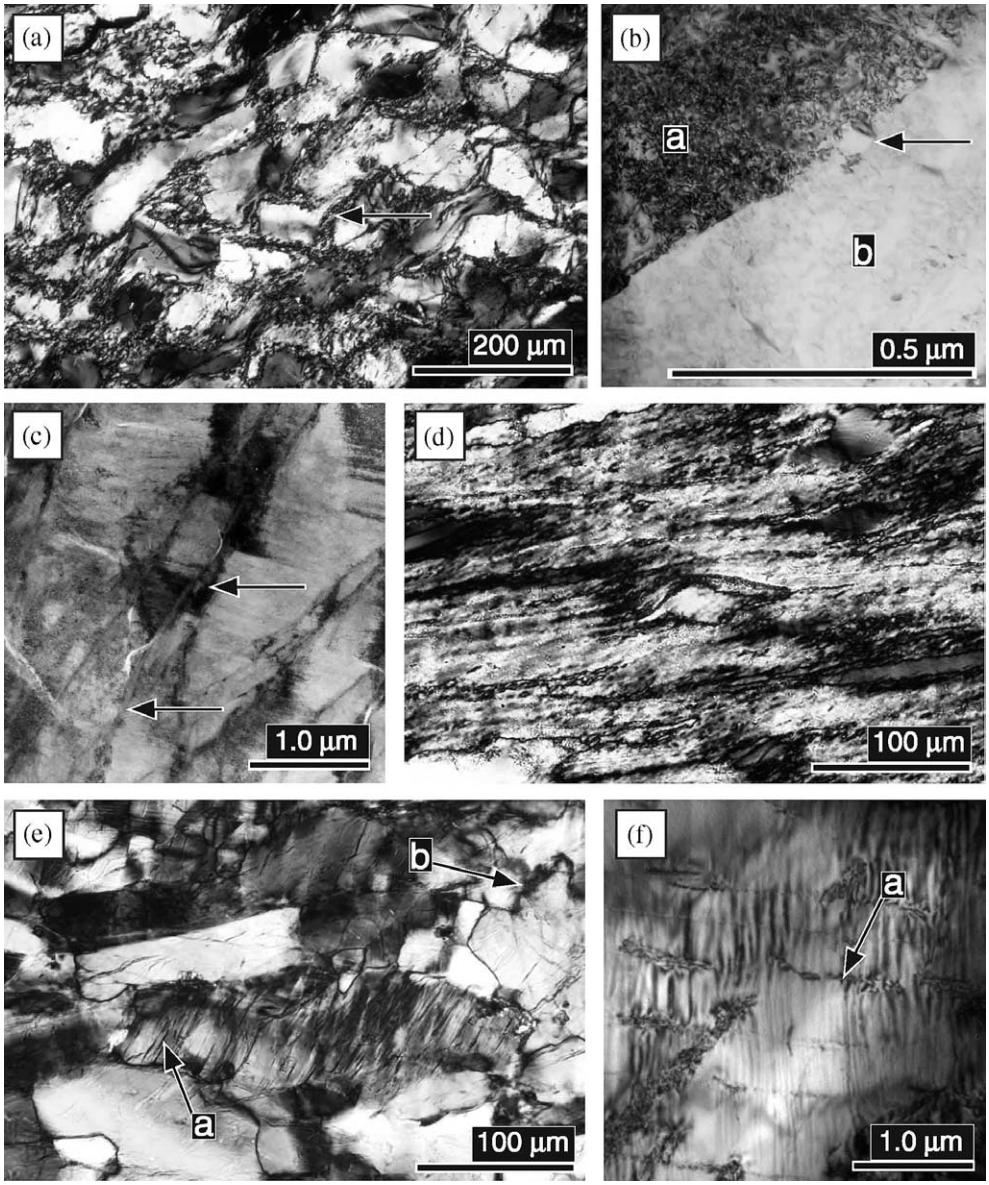

Fig. 4. Micrographs of monophase aggregates sheared at the faster strain rate ($\dot{\gamma} = 2 \times 10^{-5}$ s^{-1}). Top edges of all of the optical micrographs are parallel to the shear plane and shear sense is top to the right. (a) Optical micrograph of Black Hills quartzite, $\gamma = 2.3$. Very small recrystallized grains surround most of the porphyroclasts (arrow). No brittle microstructures were visible optically. (b) TEM showing recrystallization-accommodated dislocation creep microstructure; grain (b) with a low dislocation density has bulged into grain (a) with a higher dislocation density and formed a new strain-free grain (arrow). (c) At the TEM scale some grains have arrays of linear dislocations (E–W-trending features) and microcracks approximately perpendicular to the dislocations (arrows). (d) Optical micrograph of Black Hills quartzite, $\gamma = 6.1$. Most of the sample has recrystallized; a few small porphyroclasts remain (δ-clast in center of photomicrograph). (e) Optical micrograph of Tanco albite, $\gamma = 0.5$. Deformation occurred dominantly by cataclastic flow, with multiple faults along cleavage planes (a) and some zones of finely crushed material (b). (f) TEM microstructure showing distributed stress-bearing cracks (a), but no dislocations (a).

dominantly recrystallization-accommodated dislocation creep with some semi-brittle flow (Hirth and Tullis, 1992, 1994).

The second quartzite sample (W1105) deformed at 800F had a similar peak stress (1350 MPa); it was taken to much higher strain ($\gamma = 6.1$) and exhibited modest weakening to 910 MPa. This sample is also homogeneously deformed; it is ~90% recrystallized with only a few remaining porphyroclasts (Fig. 4d). TEM shows small (0.5–2 μm) recrystallized grains (not pictured) with a variable but high dislocation density, characteristic of recrystallization-accommodated dislocation creep.

The third quartzite sample (W1153) was deformed at 745S; its peak strength was 770 MPa ($\gamma = 0.8$) and it weakened to 400 MPa by $\gamma = 2.7$. The sample is ~60% recrystallized and the recrystallized grains are ~2 μm. Both equant and ribbon-shaped porphyroclasts were observed. These microstructures are characteristic of dominantly recrystallization-accommodated dislocation creep with a minor late component of climb resulting from strain weakening.

One experiment (W1117) was performed at 800F on Tanco albite oriented with its foliation parallel to the shear plane. The sample was very strong (1430 MPa); it was strained to $\gamma = 0.9$. Both grain-scale faulting along cleavage planes and thin zones of extremely fine-grained material were observed (Fig. 4e). At the TEM scale, porphyroclasts contain closed cracks with strain contrast along their length (Fig. 4f) and zones of finely crushed grains (not pictured); no dislocations were observed. An additional experiment was performed at 745S and the peak strength and microstructures were the same as those observed in the 800F sample. These microstructures are consistent with cataclastic flow (Tullis and Yund, 1987, 1992).

3.2.2.2. Polyphase aggregates. Seven experiments were performed on the Gneiss Minuti at the 800F and 745S conditions from low to high strains, to determine the variation of microstructures during weak phase interconnection and strain localization. Based on the peak strengths of the Black Hills quartzite experiments and predictions from the flow law

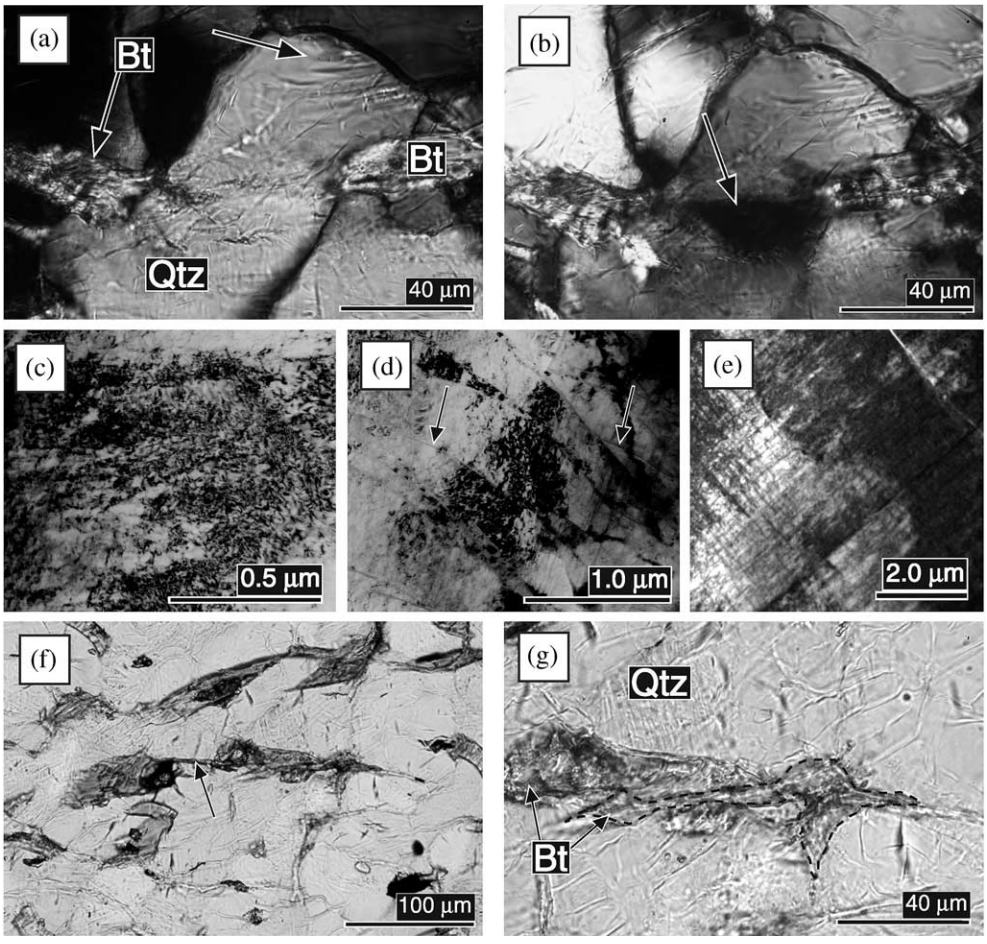

Fig. 5. Micrographs of the 800F high PSC Gneiss Minuti sample deformed to low strain ($\gamma = 1.1$). Top edges of all optical micrographs are parallel to the shear plane and shear sense is top to the right. Mineral abbreviations are: Qtz for quartz, Pl for plagioclase, Bt for biotite, Gt for garnet, RP for reaction products. Optical micrographs (a) and (b) show the same quartz grain between two adjacent biotite grains, under crossed nicols, but with the polarizers rotated 45°. The band in the center of the grain goes to extinction ~17° from most of the rest of the grain (arrow in (b)). Outside of this band deformation lamellae are locally developed (arrow in (a)). (c) TEM micrograph of quartz grain not adjacent to biotite grain, showing a typically high density of tangled dislocations. (d/e) TEM micrographs from portion of quartz grain between biotite grains showing (d) grain-scale fractures and (e) orthogonal arrays of linear dislocations. (f) Optical micrograph of a biotite grain that has been kinked and sheared (arrow). (g) Detail of the grains sheared into contact in (f). The outline of one of the biotite grains is traced by a dashed line.

for biotite (Kronenberg et al., 1990), the strength contrast between the quartz-dominated LBF and the weak phase (biotite) is approximately 45× at 800F and ~25× at 745S. Three samples were sheared to $\gamma = 0.6$, 1.1, and 3.3 at 800F and four samples were sheared to $\gamma = 1$, 1.6, 3.1, and 4 at 745S. The microstructures in both sample sets are the same at low strain, where they follow the same stress/strain curves. However, at high strain the curves diverge and there is a corresponding divergence in the high strain microstructures. Therefore, at low and intermediate strain no distinction will be made in the description of the microstructures between the samples of the 800F and 745S sets, but the high strain microstructures of the 800F and 745S sets will be described separately. The high strain 800F sample developed a single through-going shear zone that accommodated the majority of the strain, but the high strain 745S samples deformed more homogeneously and developed a pervasive S–C′ fabrics.

Low strain. One sample in each set (W1173-745S and W1019-800F) was deformed just past the peak strength (1370 and 1330 MPa, respectively; Fig. 3d and b). Localized intragranular deformation was observed in the portions of quartz grains directly between biotite grains parallel to the shear plane. Such regions in quartz grains show intense local undulatory extinction or deformation bands (Fig. 5b). TEM of such areas shows zones of tangled dislocations cross-cut by microfractures (Fig. 5d) or by perpendicular sets of linear dislocations (Fig. 5e). A few grain-scale faults lined with sheared biotite are also present (Fig. 5f). Quartz grains or portions of grains that are not directly between biotite grains contain deformation lamellae (Fig. 5a) and sutured quartz–quartz grain boundaries; TEM of these regions shows high densities of tangled dislocations. The microstructures indicate that quartz in between biotite grains deforms by semi-brittle flow, but elsewhere it deforms by recrystallization-accommodated dislocation creep. Biotite grains deform primarily by slip and kinking on (001). Most biotite grains contain kinks (Fig. 5a); a very few grains have undergone extensive slip where grain-scale faulting of quartz or feldspar has occurred (Fig. 5f). Plagioclase grains located between biotite grains parallel to the shear plane have developed local grain-scale faults whereas those not directly adjacent to biotite grains remain undeformed. SEM analyses of these samples showed no reaction products.

Intermediate strain. One sample in each sample set (W1173-745S and W1019-800F) was taken to an intermediate strain ($\gamma = 1.6$ and 1.1, respectively). The peak strengths (1190 and 1300 MPa, respectively) were somewhat lower than those of the low strain samples, and the samples rapidly strain-weakened after yielding (Fig. 3b and d). Offsets along grain-scale faults in quartz and plagioclase, which allowed biotite interconnection, are larger and more numerous than in the low strain samples (Fig. 6a). In these zones biotite grains are highly strained (Fig. 6a). Microstructures observed in quartz and plagioclase grains in these samples are not significantly different from those observed in the low strain samples. The quartz grains are more recrystallized than in the low strain samples and they contain no microfractures, indicating that they deformed by recrystallization-accommodated dislocation creep. Biotite grains in the high strain zones are sheared along (001) and kinked. In the 800F sample there are extremely fine-grained (1–3 μm) reaction products (Fig. 6b) at the edges of high strain regions of a few biotite grains. The reaction products are only observed in high strain portions of biotite grains and occupy $\ll 1\%$ of the total sample volume. The reaction products are too fine-grained to accurately analyze using SEM techniques.

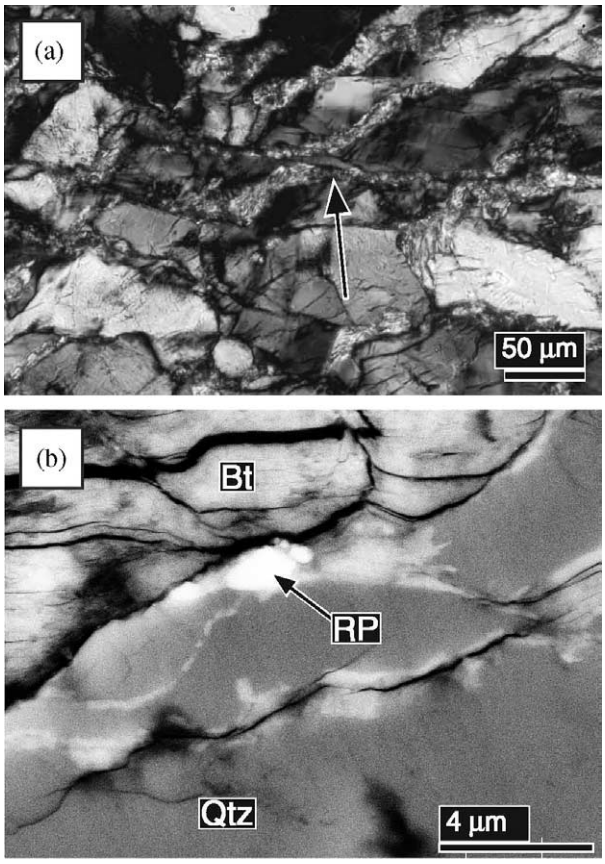

Fig. 6. Micrographs of intermediate shear strain high PSC Gneiss Minuti sample ($\gamma = 1.1$). Top edges of both micrographs are parallel to the shear plane and shear sense is top to the right. (a) Optical micrograph of highly sheared and locally interconnected biotite (arrow). (b) SEM BSE image of a reaction product formed in the high strain zone of a biotite grain.

High strain. Three samples were sheared to high strains (W1139/W1156-745S and W1008-800F) of $\gamma = 3.1$, 4, and 3.3, respectively (Fig. 3d and b). They had essentially the same peak strengths and weakening curves as the intermediate strain samples and weakened to 640, 730, and 510 MPa at $\gamma = 2.2$, 2.2, and 2.6, respectively, and deformed at nearly constant stress until the completion of the experiments. As noted previously, the two sample sets no longer contain the same microstructures or fabric. We will first describe the microstructures observed in the 745S samples and then those observed in the 800F sample.

In the 745S samples many strands of multiply interconnected biotites are found throughout the sample (Fig. 7a), but there is no single through-going shear zone in the sample. The biotites define an S–C′ fabric. At the optical scale quartz

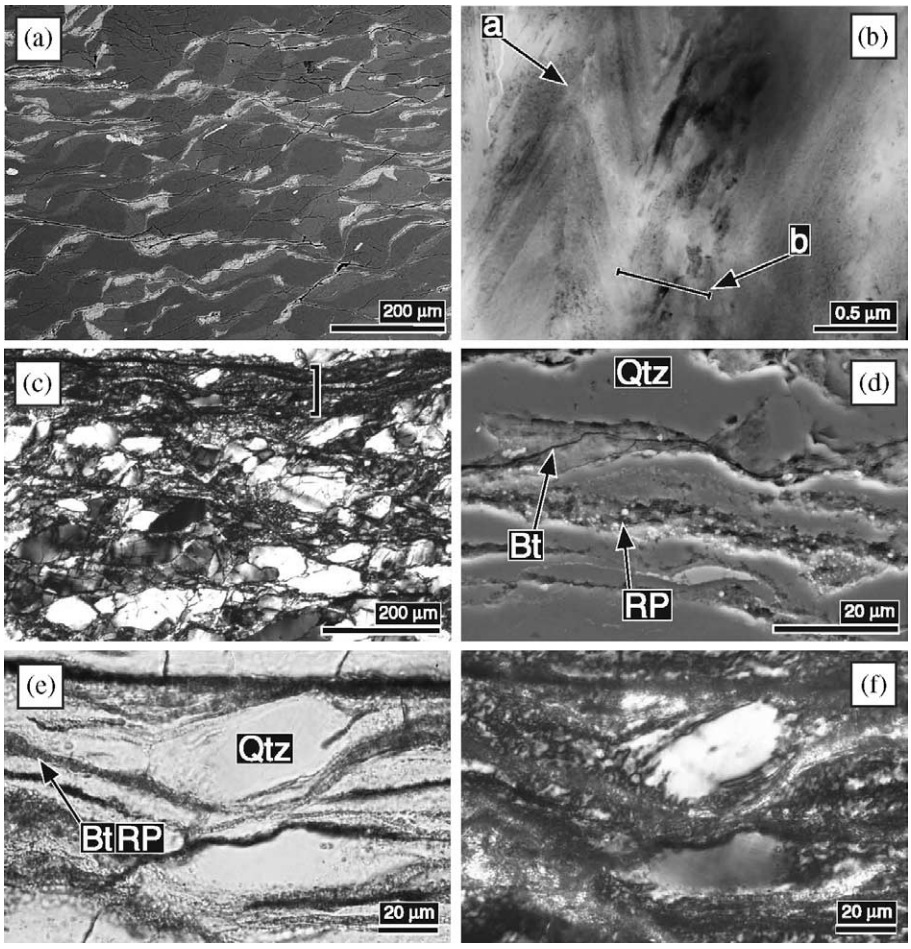

Fig. 7. Micrographs of high shear strain high PSC Gneiss Minuti samples. Top edges of all micrographs are parallel to the shear plane and shear sense is top to the right. (a) BSE SEM image of the many interconnected biotite strands in the high strain 745S sample ($\gamma = 3.1$). (b) TEM image showing (a) hinges of biotite kinks and (b) zone of fine-grained recrystallized biotite in the hinge of a kink in the high strain 745S sample. (c) Optical micrograph of the narrow shear zone (bracket) that has developed in the high strain 800F sample (thickness 75–100 μm, $\gamma = 3.3$). (d) SEM-SE micrograph of biotite, reaction products and quartz within the shear zone. Within the Bt/RP layer, lighter spots are reaction products mixed in with darker highly strained biotite. (e) Plane polarized and (f) crossed nicols optical micrographs of the quartz porphyroclast and layers of biotite/reaction products (Bt/RP) in shear zone in (c).

porphyroclasts are equant and have undulatory extinction. At their edges are very small recrystallized grains. At the TEM scale quartz porphyroclasts contain high densities of curved dislocations and are surrounded by small ($\sim$1–2 μm) recrystallized grains that also contain variable densities of curved dislocations. These microstructures are indicative of dominantly recrystallization-accommodated dislocation creep, with a small component of climb. Plagioclase porphyroclasts contain mechanical twins and are surrounded by very small strain-free recrystallized grains. At the TEM scale, biotite grains appear to be recrystallizing, with new grains ($<$0.5 μm) observed in kink hinges (Fig. 7b).

In the 800F high strain sample, a single narrow (75–100 μm) through-going shear zone begins near one corner of the upper shear piston, continues parallel to the shear piston $\sim$3/4 across the sample, and then cuts obliquely across the sample and connects to the opposite corner of the lower shear piston (Fig. 7c). The narrow shear zone accommodated the majority of strain. Outside of the shear zone a weak S–C′ fabric has developed (Fig. 7c). The microstructures outside the shear zone are different and described separately from those inside the shear zone.

Outside of the shear zone, quartz porphyroclasts are moderately flattened and have a shape preferred orientation; they contain deformation lamellae and patchy extinction, and have sutured grain boundaries with small recrystallized grains (Fig. 7c). TEM shows that porphyroclasts have some curved dislocations, dislocation arrays (not pictured) and serrated grain boundaries with small ($\sim$1–2 μm) polygonal dislocation-free grains. These microstructures are consistent with dislocation creep that is transitional between regimes 1 (recrystallization-accommodated) and 2 (climb-accommodated) (Hirth and Tullis, 1992). Biotite grains contain a few kinks; they are partially reacted along their edges, but not in their centers. Plagioclase grains contain some closed cracks with strain contrast along their length and few dislocations (not pictured).

Within the shear zone quartz is mostly recrystallized, forming fine-grained layers with a few remaining small ($<$30 μm) porphyroclasts (Fig. 7e and f). Biotite is very

fine-grained and contains ~30% reaction products, including 1–5 μm garnet and Fe/Ti oxides, which are well mixed with fine-grained biotite (Fig. 7d). Many of the biotite (001) are no longer parallel to the shear plane, possibly reflecting some of the sliding motions or rotations necessary to accommodate strain during grain boundary sliding.

3.2.3. Low phase strength contrast experiments

3.2.3.1. Monophase aggregates. One sample of Black Hills quartzite was deformed at the slower strain rate to $\gamma = 3.7$; the peak stress was 290 MPa and the steady state flow stress was ~160 MPa. The sample is homogeneously deformed and almost completely (~95%) recrystallized, with only a few small porphyroclasts remaining (Fig. 8a). TEM of recrystallized grains shows that they vary in size from 4 to 8 μm and have a low density of curved dislocations, a few dislocation arrays and curved grain boundaries (Fig. 8b), indicating deformation by climb-accommodated dislocation creep. A sample of Tanco albite had a peak strength of 1150 MPa ($\gamma = 0.5$) and it strain hardened to 1740 MPa by $\gamma = 4.2$. Deformation is concentrated within thin zones of fine grains oriented ~25° clockwise from the shear plane (Fig. 8c). TEM observations of mixed cracks and dislocations in grains within such zones (not pictured) indicate that semi-brittle flow is the dominant deformation mechanism. Porphyroclasts outside of these zones have closed cracks with strain contrast along their length and few dislocations (Fig. 8d).

3.2.3.2. Polyphase aggregates. Three samples of the Gneiss Minuti were sheared to strains of $\gamma = 0.6$, 1.5, and 5.4 at the 800S conditions. Based on the peak strength of the Black Hills quartzite sample and the biotite strength predicted from the flow law of Kronenberg et al. (1990), the strength contrast between the quartz-dominated LBF and the weak phase (biotite) is only ~10× at the slower strain rate.

Low strain. One sample (W-1076) was strained to $\gamma = 0.6$, just past the peak stress of 650 MPa (Fig. 4f). The sample is homogeneously strained, with quartz accommodating the majority of the deformation. Only one clear case of localized intragranular strain was observed, in a plagioclase grain adjacent to a biotite grain. Quartz–quartz grain boundaries are sutured and contain small (~1 μm) dislocation-free recrystallized grains, and TEM shows regions of tangled dislocations as well as a few dislocation arrays (Fig. 9b). Biotite grains have slipped on (001), with minor kinking at their edges (Fig. 9a). At some quartz–quartz grain boundaries, strain localized along the weak recrystallized grains, causing the quartz porphyroclasts to shear along these boundaries. Biotite grains were passively sheared on (001) along with the adjacent quartz porphyroclasts and end up between the adjacent quartz porphyroclasts (Fig. 9a). TEM observations of plagioclase grains show high dislocation densities and zones

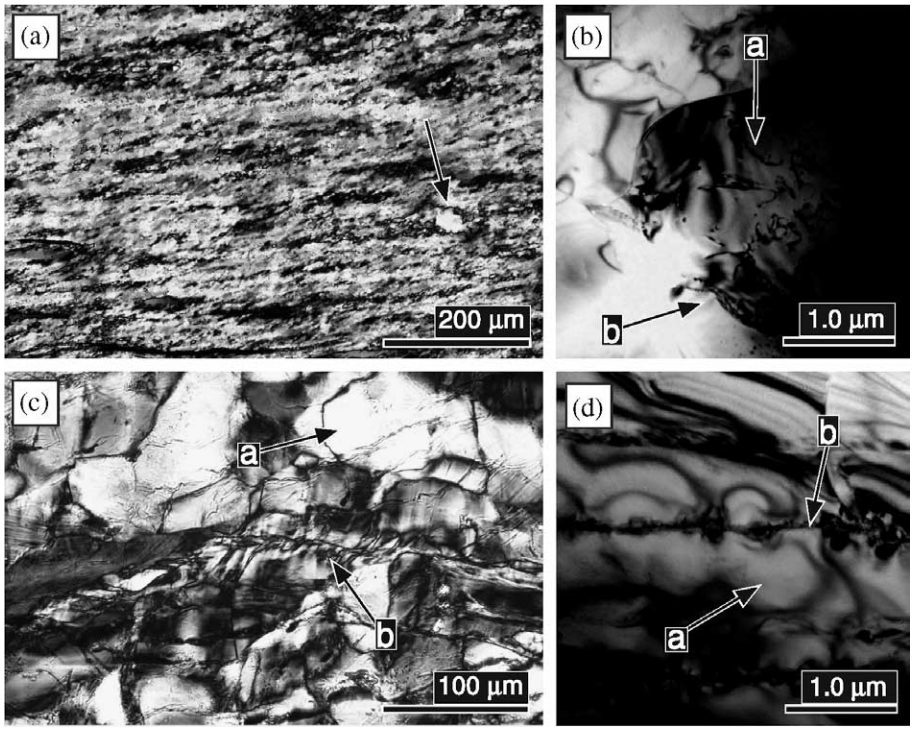

Fig. 8. Micrographs of monophase aggregates sheared at the slower strain rate ($\dot{\gamma} = 2 \times 10^{-6}\ s^{-1}$). Top edges of all of the micrographs are parallel to the shear plane and shear sense is top to the right. (a) Optical micrograph of Black Hills quartzite, $\gamma = 3.7$. The majority of the sample is completely recrystallized with few porphyroclasts remaining (arrow). (b) TEM micrograph of quartz showing a low density of curved dislocations (a), indicating climb is the dominant recovery mechanism; recrystallized grains are not polygonal, but have curved edges (b). (c) Optical micrograph of Tanco albite, $\gamma = 4.2$, showing evidence of semi-brittle flow. There are some relatively undeformed porphyroclasts (a) and thin zones of finely crushed and/or recrystallized material (b). (d) TEM micrograph of Tanco albite showing dislocation-free regions (a) with multiple stress-bearing cracks (b).

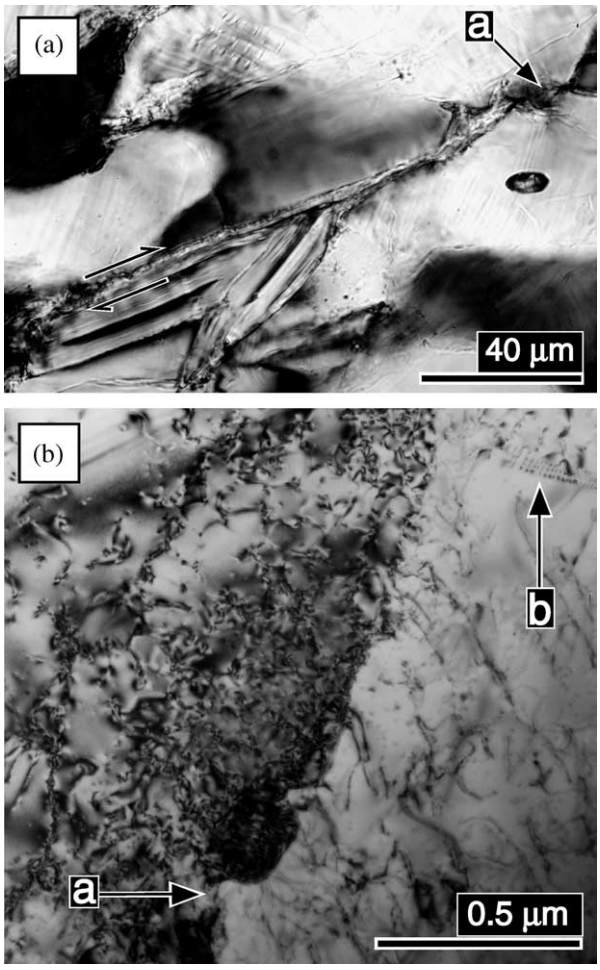

Fig. 9. Optical micrographs of low shear strain low PSC Gneiss Minuti sample ($\gamma = 0.6$). Top edges of all micrographs are parallel to the shear plane and shear sense is top to the right. (a) Biotite grain that has been sheared into a recrystallized quartz–quartz boundary (a). (b) TEM image of quartz, showing grain boundary bulging (a) from a lower into a higher dislocation density region. Occasional dislocation walls (b) are also present in quartz grains in this sample.

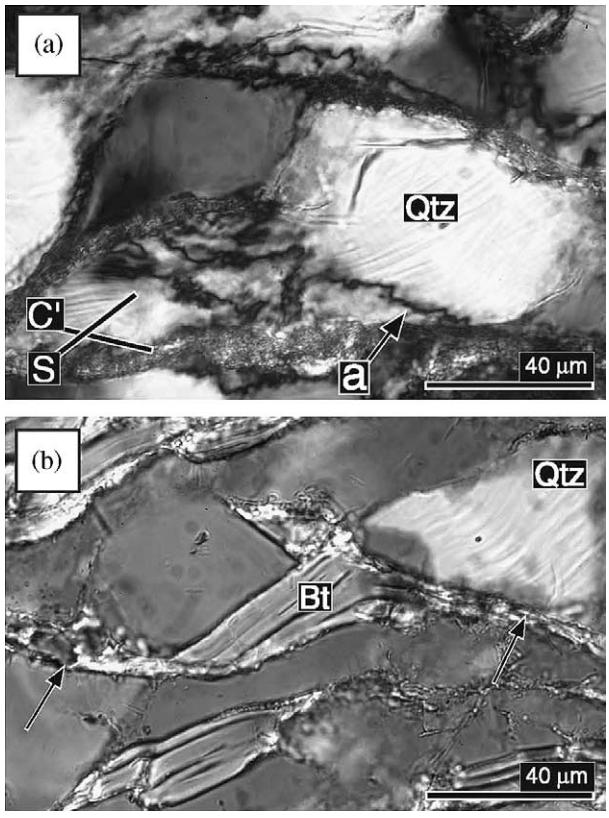

Fig. 10. Micrographs of intermediate shear strain low PSC Gneiss Minuti sample ($\gamma = 1.5$). Top edges of all micrographs are parallel to the shear plane and shear sense is top to the right. (a) Optical micrographs showing recrystallized quartz in the C′ shear bands (a). (b) Optical micrograph of the undeformed portion of a biotite grain rotated into the S orientation and the sheared portions of the biotite grain in the C′ orientation.

of finely crushed and/or recrystallized grains, indicating semi-brittle flow. No reaction products were observed in SEM analyses of this sample.

Intermediate strain. One sample (W-1079) was strained to $\gamma = 1.5$; its peak strength was 520 MPa and it strain weakened to 230 MPa (Fig. 4f). Multiply interconnected strands of biotite occur throughout the sample, but none are through-going. A weak S–C′ fabric has started to develop (Fig. 10a and b). Quartz grains are slightly flattened, with strongly sweeping undulatory extinction. Deformation lamellae are common, and quartz–quartz grain boundaries are sutured and recrystallized (Fig. 10a). At the TEM scale, dislocation arrays and small ($\sim$1–2 μm) low dislocation density recrystallized grains are common (not pictured). Biotite grains are more highly strained in this sample than in the low strain sample; the majority of grains appear to have deformed by slip along (001) with some kinking. There are thin zones of highly strained biotite and reaction products in high strain zones in between framework grains (Fig. 10b). The centers of the biotite grains are relatively undeformed and in some cases have been rotated into the S orientation while the sheared ends define the C′ orientation of the S–C′ fabric (Fig. 10b). In the plagioclase grains, TEM shows high densities of tangled dislocations and very fine (<1 μm) crushed and/or recrystallized grains (not pictured).

High strain. One sample (W-1020) was sheared to $\gamma = 5.4$; it has essentially the same flow strength (200 MPa) as the lower strain sample, but much higher strain. The sample is homogeneously deformed with multiple zones of thoroughly mixed biotite/reaction products surrounding highly recrystallized ribbon quartz grains (Fig. 11a). In the TEM, quartz grains show low dislocation densities and many dislocation arrays (Fig. 11d). Some polygonal, strain-free recrystallized grains ($\sim$3–5 μm) were also observed. The porphyroclasts remaining are plagioclase with minor sweeping extinction and long tails of recrystallized grains. In the TEM, small dislocation-free recrystallized grains (<1 μm) were observed along the boundaries of high-dislocation density plagioclase porphyroclasts. Biotite and reaction products are thoroughly mixed within interconnected layers. These layers are parallel to the shear plane and define the C (not C′) plane in the penetrative S–C fabric in the high strain sample (Fig. 11b), but local zones of S–C′ exist about porphyroclasts (Fig. 11c).

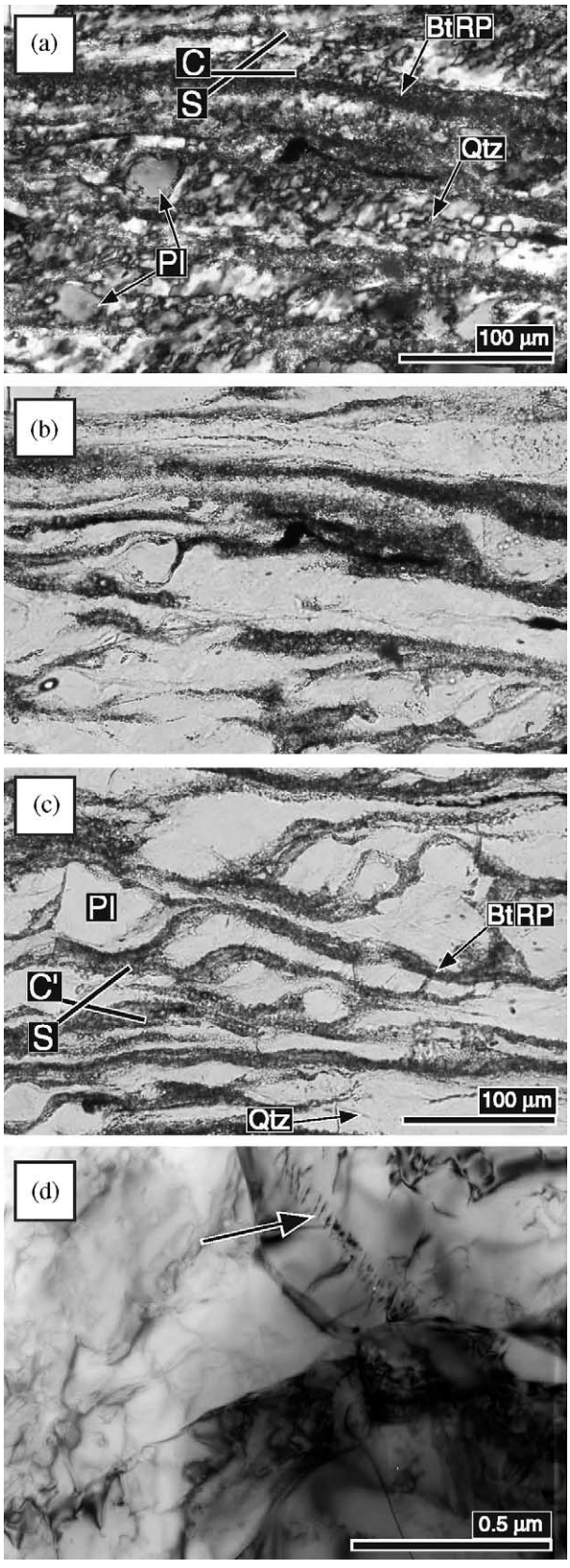

Fig. 11. Micrographs of high shear strain low PSC Gneiss Minuti sample ($\gamma = 5.4$). Top edges of all micrographs are parallel to the shear plane and shear sense is top to the right. (a) Crossed nicols micrograph of quartz grains that are highly recrystallized. There are multiple through-going biotite and reaction product layers in the C plane. The S plane is dominantly defined by the long direction of the recrystallized quartz grains. (b) Plane polarized light micrograph of the same area. (c) Plane polarized light micrograph of a region in the sample that contains several plagioclase clasts and forms a local zone of S–C′ fabric, although several biotite/reaction product layers are in the C orientation. (d) TEM image of recrystallized grains of quartz showing dislocation arrays (arrow) and a low dislocation density.

4. Discussion

4.1. Estimates of stress concentrations

In all of the deformed Gneiss Minuti samples, most of the load is initially borne by the quartz–plagioclase framework, because the biotites are in their weakest easy slip orientation. In the HPSC samples the microstructures observed in the quartz grains vary strongly with their location relative to biotite grains, reflecting the local stresses. In the low strain HPSC samples, the deformation microstructures in quartz grains away from the tip ends of biotite grains are indicative of high-stress recrystallization-accommodated dislocation creep (Hirth and Tullis, 1992). These microstructures are very similar to those observed in the Black Hills quartzite sample deformed at the same conditions, which had a similar high peak strength. In contrast, quartz grains or portions of grains located between biotite grains aligned parallel to the shear plane have microstructures indicative of the higher stress process of semi-brittle flow (Hirth and Tullis, 1994). This localized semi-brittle deformation allowed for grain-scale faulting of the most highly stressed quartz grains, which in turn allowed the biotites on either side to become interconnected via easy slip on (001). This observation indicates that the local stresses at the ends of the weak biotite grains are significantly higher than those elsewhere in the sample. The peak strengths of quartzite deformed by semi-brittle flow and semi-brittle faulting measured in a similar solid medium assembly are 1600–2300 MPa (Hirth and Tullis, 1994). Based on the peak strengths of the HPSC samples ($\sim$1300 MPa) and the quartz microstructures, the stress concentrations in quartz/feldspar grains at the tips of biotite grains prior to yielding are approximately 1.2–1.6$\times$ the bulk peak stress of the gneiss.

In the LPSC samples the strength contrast between the biotite and quartz grains is much lower ($\sim\times 10$), indicating that the stress concentrations at the tip ends of biotite grains are lower. At these conditions the peak strength of the Gneiss Minuti samples ($\sim$550 MPa) is considerably higher than that for the Black Hills quartzite sample ($\sim$290 MPa). The microstructures observed in quartz grains in the low strain LPSC sample indicate that they deformed primarily by recrystallization-accommodated dislocation creep, although with a small component of dislocation climb. In contrast, the Black Hills quartzite sample deformed by climb-accommodated dislocation creep. The difference in quartz deformation mechanisms between the Gneiss Minuti and Black Hills quartzite samples at low strain indicates that the stress concentrations cause higher stress deformation mechanisms to operate initially in the LPSC samples, just as in the HPSC

samples. However, the microstructures formed by recrystallization-accommodated dislocation creep occur over such a wide range of stresses (Hirth and Tullis, 1992) it is impossible to determine the stress concentrations in these samples based only on differences in microstructures.

It is of interest to calculate the approximate stress concentrations developed in the Gneiss Minuti samples, for comparison with the stress differences inferred from the variation in quartz microstructures. Recent numerical modeling by Johnson et al. (2004) predicts that for biotite grains aligned parallel to the shear plane and separated by one grain width in an en échelon array within a plagioclase matrix, the local stress concentrations would be $\sim$1.3–2$\times$ the confining pressure (e.g. 1900–3000 MPa). This model has a geometry similar to that in our Gneiss Minuti samples, and although it was limited to $\gamma = 0.03$, it predicted localized brittle failure of the plagioclase grains between adjacent biotites, just as we observe.

4.2. Effect of phase strength contrast on mechanisms of weak phase interconnection

In the HPSC samples, the stress concentrations in the strong framework phases adjacent to the weak biotite grains caused the Gneiss Minuti samples to yield by local semi-brittle flow at conditions where monophase aggregates of the framework minerals deform by recrystallization-accommodated dislocation creep. The local semi-brittle flow of quartz and plagioclase allowed the biotite grains to become interconnected by shearing along the grain-scale faults.

In the LPSC samples, the initial interconnection of biotite grains also resulted from local stress concentrations in the framework quartz grains, although it occurred by a different mechanism. In these 800S Gneiss Minuti samples, the stress concentration is a similar factor times the monophase flow stress, but it results in a local stress magnitude that remains lower than the confining pressure so that no cracking is produced. The Black Hills quartzite sample deformed by climb-accommodated dislocation creep, whereas in the low strain Gneiss Minuti sample the microstructures in quartz grains near the tips of biotite grains indicate deformation by the higher stress process of recrystallization-accommodated dislocation creep. The development of very weak (dislocation-free) recrystallized grains along quartz–quartz boundaries allowed local grain boundary shearing of the hardened quartz porphyroclasts and of adjacent biotite grains. Eventually ($\gamma = 1$) thin zones of biotite and recrystallized quartz completely separate the framework porphyroclasts.

Several previous experimental studies have investigated the processes and consequences of interconnection of an initially isolated weak phase within a stronger framework. In studies somewhat similar to ours except conducted at lower pressure and temperature where all framework phases deformed in a brittle manner, Gottschalk et al. (1990), Shea and Kronenberg (1993), and Rawling et al. (2002) deformed quartz–feldspar rocks with varying percentage and alignment of micas, in axial compression. Based on monophase aggregate strengths published by Tullis and Yund (1992), Hirth and Tullis (1994), and Kronenberg et al. (1990), the PSC was probably between $\sim$27$\times$ (feldspar–easy slip biotite) and 52$\times$ (quartz–easy slip biotite). In experiments performed with mica (001) at 45° to σ_1, low strain samples with isolated mica grains developed high densities of microcracks in quartz and feldspar grains at the tips of mica grains, but not in other locations, and with continued loading this localized cracking lead to through-going fractures. Since the deformation of monophase aggregates at these conditions is already brittle, it is not surprising that stress concentrations lead to enhanced cracking of the quartz–plagioclase framework and subsequent local interconnection of the weak micas.

A different study was performed on aggregates of stronger calcite with initially isolated weaker halite (Jordan, 1987); these aggregates had a much lower PSC (approximately 5–7$\times$), but monophase aggregates of the framework phase again were brittle at the experimental conditions chosen. Thus, it is not surprising that the stress concentrations in calcite grains adjacent to the weak halite inclusions caused local enhancement of brittle deformation, allowing interconnection of weak halite. Strain was partitioned into the weaker halite after it became interconnected, both in axial compression and in shear.

A somewhat similar experimental study was performed by Dell'Angelo and Tullis (1996) on Enfield aplite, which has 33% quartz grains isolated within a feldspar (66%) matrix. For experiments performed at 900 °C, 1500 MPa and an axial strain rate of 2×10^{-6} s^{-1}, the PSC between the weaker quartz and stronger feldspars was about 2.4$\times$. At these conditions pure feldspar aggregates deformed by recrystallization-accommodated dislocation creep. Dell'Angelo and Tullis (1996) inferred that the initial interconnection of the weaker quartz was due to localized grain boundary shearing associated with development of strain-free recrystallized grains along feldspar grain boundaries. The process is very similar to the one we observe in our LPSC samples.

To summarize, the magnitude of the stress concentration adjacent to isolated weak phases is directly related to the PSC between the phases. However, whether that stress concentration causes local brittle deformation or local higher stress crystal plastic deformation depends on how close the stronger framework phases are to brittle behavior without the extra stress concentrations. Thus, in some cases a high PSC may still allow crystal plastic deformation of the framework to cause interconnection of weak phases, whereas in other cases a low PSC may be sufficient to cause brittle failure of the framework and subsequent local interconnection of weak phases.

4.3. Effects of phase strength contrast on the degree of strain localization

In addition to affecting the mechanisms of weak phase interconnection in polyphase rocks, the PSC between the weak phase and the strong framework, and the way in which it may change with progressive strain, affects the degree of strain localization. Our three sample sets illustrate different degrees

of strain localization, due to differences in the initial and the evolving PSC.

The highest degree of strain localization occurs in the high strain 800F sample, which has the highest initial PSC (45×) between the quartz framework and the weak biotite and which maintains the high PSC with increasing strain. After initial interconnection of biotite grains by grain-scale faulting of framework grains resulting from local stress concentrations, the elongated zone of weak biotite has a larger aspect ratio and thus a higher stress concentration at its tip. At the same time, biotite grains begin to kink, and this process rotates (001) into harder orientations, increasing the strength of the biotite and thus decreasing the PSC. However, in these 800 °C HPSC samples, highly strained regions of biotite grains undergo dehydration reaction, forming very fine-grained reaction products (including garnet and Fe/Ti oxides; Fig. 6). The local reaction of biotite increases the PSC and promotes further strain localization in two ways. First, the reaction produces a zone of fine-grained, mixed-phase material that deforms by diffusion-accommodated grain boundary sliding, and the localized strain in turn enhances further reaction progress within the localized zone. Diffusion-accommodated grain boundary sliding is inferred because the initial appearance of reaction products is at the kinked edges of highly strained biotite grains, but with increasing strain the reaction products are thoroughly mixed with fine-grained biotite. Second, the water of dehydration may cause hydrolytic weakening of the quartz and plagioclase within the shear zone. More details of the microstructural evolution of the biotite/reaction product layers are presented in Holyoke and Tullis (submitted). Thus, localized strain leads to localized reaction, which in turn maintains a HPSC and thus maintains localized strain.

The 745S samples have a lower degree of strain localization than the 800F samples, due to a decrease of the initially high PSC (25×) between biotite and the quartz–plagioclase framework with increasing strain. The initial stages of deformation are similar to those of the 800F samples: stress concentrations allow initial interconnection of biotite by local grain-scale faulting of the framework phases, but then kinking of biotite grains tends to strengthen them by rotating their (001) into harder orientations. In the experiments of Kronenberg et al. (1990), the strength of biotite with (001) perpendicular to σ_1 is about an order of magnitude larger than that for (001) at 45° to σ_1, which is similar to the difference between peak strength and final strength after strain weakening in the biotite aggregates deformed at the 800F conditions. The lower degree of strain localization in the 745S samples results because in the lower temperature samples there is very little biotite reaction to offset the kink-strengthening, and so the PSC decreases with increasing strain, to a value between 7 and 3×, based on the yield strengths of biotite experiments performed at the 800S and 800F conditions and the Black Hills quartzite experiment performed at the 745S conditions. During strain weakening in these samples, strain appears to be progressively repartitioned to other relatively unkinked biotite grains that still have a high PSC with the framework, until at high sample strain there are many zones of interconnected and kinked biotite (Fig. 7a).

The 800S samples have the least strain localization, because they have the lowest initial PSC (10×) and it appears to decrease with progressive strain. The relatively low peak strength of the framework quartz at these conditions and the low PSC means that the initial process of biotite interconnection involves grain boundary shearing along zones of weak recrystallized quartz grains rather than grain-scale faulting. This grain boundary shearing occurs fairly homogeneously along many quartz–quartz boundaries in the sample, leading to multiple zones of interconnected biotite at fairly low sample strain. At the same time, biotite dehydration produces fine-grained, mixed phase reaction products that appear to undergo diffusion-accommodated grain boundary sliding; the reaction also releases water that should cause hydrolytic weakening of the framework grains. The quartz grains are highly flattened and recrystallized, although plagioclase grains remain less deformed. Paleopiezometry in the recrystallized quartz grains in the high strain sample indicates a flow stress of 180 MPa (Stipp and Tullis, 2003), giving a strain rate in the quartz grains of $1.6\times10^{-6}\,s^{-1}$ using the flow law of Gleason and Tullis (1995). This strain rate is approximately the same as the bulk strain rate in the sample ($2.3\times10^{-6}\,s^{-1}$), indicating there is very little strain partitioning between the quartz and the biotite/reaction products, consistent with a very low PSC.

Other experimental deformation studies offer some comparisons. Bons and Cox (1994) deformed an aggregate with weaker octochloropropane (OCP) in a matrix of stronger camphor (PSC ~ 30×) in rotary shear. After the weaker OCP became interconnected (mechanism not specified), the sample initially strain weakened, but almost immediately it strengthened due to folding of the OCP phase. This process is similar to the strengthening in our HPSC samples, which was caused by the kinking of biotite.

Tullis and Wenk (1994) investigated strain partitioning in hot-pressed quartz–muscovite aggregates deformed in axial compression at 800 °C and 1500 MPa; they used samples of varying muscovite content at two different strain rates. At the faster strain rate the PSC was about 20× and for muscovite contents sufficient to coat almost all quartz grain boundaries (e.g. >15%) the sample strain was largely partitioned into the muscovite, leaving the volumetrically dominant quartz grains almost undeformed. However, at the slower strain rate the PSC was only about 2× and for similar amounts of muscovite sufficient to coat all quartz grain boundaries, the quartz grain strain was almost the same as the sample strain. In part due to the axial compression geometry, even the samples with significant strain partitioning did not develop sample-scale strain localization.

In all of these studies, the early strain localization depends on an initially high PSC between the weak phase and the framework, but the subsequent extent of strain localization depends on the evolution of that PSC. If the initially interconnected weak phase strengthens, as by kinking of the biotite in our samples, then strain will be repartitioned into adjacent zones of unkinked material, causing new biotite interconnections. Thus, a relatively homogeneous sample strain may result, although it developed incrementally and

non-homogeneously, by a series of small-scale strain localization events.

4.4. Effects of phase strength contrast on fabric development

It is worthwhile to consider the influence of the PSC on the development of S–C or S–C′ fabrics in deformed polyphase aggregates. We are primarily interested in the processes that form these fabrics in shear zones in a transpressional (or general shear) environment. In natural rocks it has been observed that S–C fabrics develop when sample strain is relatively homogeneous (e.g. Berthe et al., 1979; Lister and Snoke, 1984; Goodwin and Tikoff, 2002), whereas S–C′ fabrics tend to develop when strain is more inhomogeneously partitioned into weaker phases (e.g. Berthe et al., 1979; Goodwin and Tikoff, 2002). We see these same fabrics in our experimental general shear samples, allowing us to provide some insights.

In our 800F samples, with the highest initial PSC, the strain is so highly partitioned into a very narrow through-going ductile shear zone that the material outside was only weakly strained and developed a weak S–C′ fabric as the sample thinned (Figs. 7c and 12a). The initial high PSC was maintained to high strain by the switch in deformation mechanisms in the biotite from (001) slip and kinking to reaction-induced diffusion-accommodated grain boundary sliding.

In the 745S samples, with the next highest initial PSC, biotite kinking and the absence of reaction caused a decrease in the PSC with increasing strain, which in turn produced more homogeneously distributed strain than in the 800F samples. Strain is primarily accommodated by biotite deformation ((001) slip and kinking), but there are multiple interconnected zones rather than a single through-going zone. The interconnected and sheared biotite zones define a C′ plane (Fig. 7a), whereas less strained biotite grains and flattened quartz and plagioclase porphyroclasts define the S plane (Figs. 7a and 12b). Thinning in these samples is accomplished by shearing along the weak material in the C′ planes and minor intracrystalline strain of the quartz porphyroclasts.

In the 800S samples, with the initially lowest PSC, the fabric development is more complex, evolving from an S–C′ fabric that forms at a PSC of about 10× in the low/mid-strain samples to an S–C fabric as the PSC and strain localization decrease at high strain. The initial shearing along recrystallized quartz–quartz boundaries forms an S–C′ fabric; the long axes of porphyroclasts of all three minerals define the S plane whereas the sheared zones of recrystallized quartz grains and interconnected biotite define the C′ plane (Figs. 10a–c and 12b). However, with increasing strain, dehydration reaction of the biotite hydrolytically weakens the entire quartz framework, reducing the PSC between the quartz and the biotite reaction products. Thus, at high sample strain an S–C fabric develops; the long axes of recrystallized quartz grains define the S plane, and bands of recrystallized quartz plus mixed biotite and reaction products define the C plane (Figs. 11a and b and 12c).

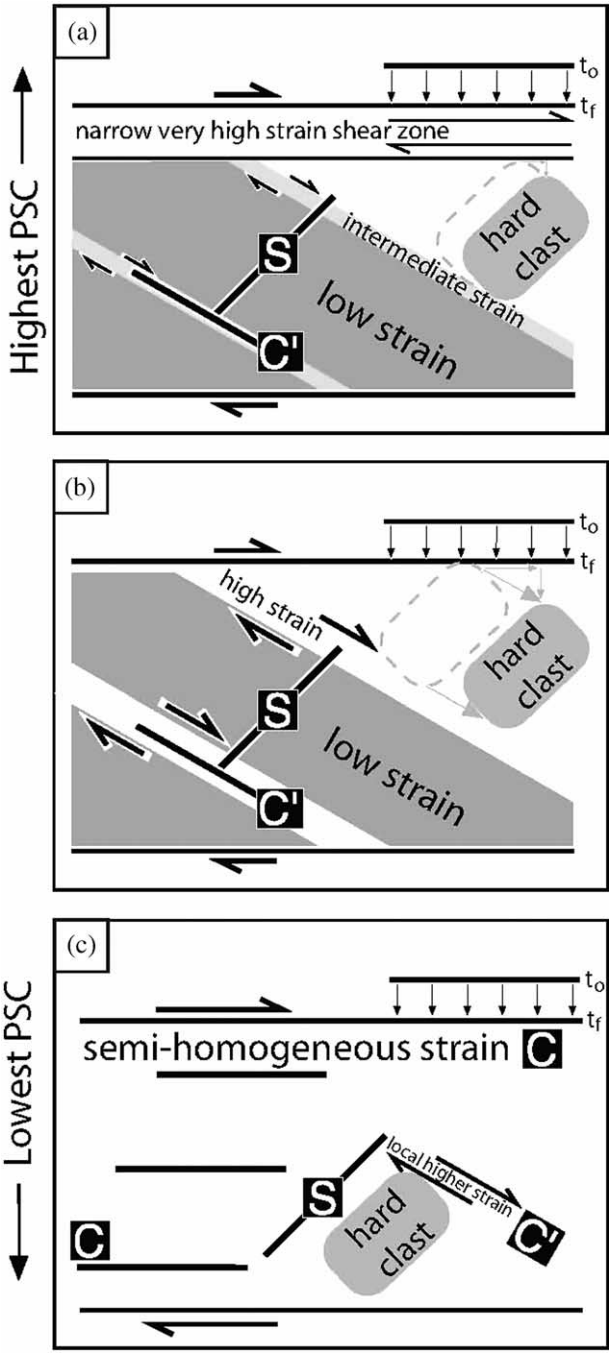

Fig. 12. (a) Schematic diagram of strain partitioning at the highest PSC. t_o and t_f are the initial and final thicknesses of the shear zone in all diagrams. The majority of sample strain is accommodated by shear within a narrow zone of very weak material. Outside of the shear zone the strain is low; it occurs by a combination of minor intracrystalline strain of the porphyroclasts and localized shear in the C′ bands that accommodates both thinning and shear strain. (b) Schematic diagram of S–C′ fabric developed at intermediate PSC. Most strain is partitioned into the C′ bands (white) and many hard porphyroclasts remain. Thinning is accomplished by localized shear in the C′ planes and minor intracrystalline strain of the porphyroclasts. (c) Schematic diagram of S–C fabric developed at very low PSC. Strain within the shear zone is relatively homogeneous, except where relic hard clasts cause local strain heterogeneities and fabric perturbations. The S plane is usually defined by the long axes of recrystallized grains or remnant porphyroclasts and the C plane is usually defined by micas or other slightly weaker phases. Thinning is accommodated by homogeneous intracrystalline strain. Zones of localized shearing in C′ planes occur adjacent to hard porphyroclasts.

However, the isolated plagioclase porphyroclasts remain significantly stronger, and cause perturbations in the fabric that are seen as strain localizing in C′ planes around these clasts (Figs. 11c and 12c). At low strain, thinning in the 800S samples is accomplished primarily through localized shearing along the C′ planes, but as the quartz weakens thinning is accomplished by homogeneous intracrystalline strain of the quartz framework.

Several other experimental studies on two-phase aggregates deformed in shear provide useful comparisons to our study. Stuenitz and Tullis (2001) sheared aggregates of plagioclase with traces of water at conditions where the plagioclase partially reacted to zoisite, white mica, quartz and kyanite; the reaction products were extremely fine-grained and deformed by diffusion-accommodated grain boundary sliding. Strain was localized into these very weak reaction products on C′ planes, while the stronger remaining plagioclase grains and large zoisite grains were less deformed and defined the S plane. The PSC between the plagioclase and the reaction products is not known exactly but must be relatively high (>10). Similarly, Jordan (1987) observed that in sheared halite–calcite aggregates (PSC ~ 5–$7\times$) strain localized primarily into halite-filled shear bands in a C′ orientation, with minor localization on the C plane and slightly elongate calcite porphyroclasts defining the S plane. In experiments performed on halite/kaolinite mixtures with a PSC of $\sim 5\times$, Bos and Spiers (2001) observed that strain was localized into bands of fine-grained kaolinite/halite mixtures along C′ planes whereas large halite clasts define the S plane. Holtzman et al. (2003) performed a series of experiments on olivine/chromite/basalt aggregates and also observed localization of strain in bands of melt and olivine in the C′ orientation, which they believe deformed by melt-assisted diffusion creep, whereas the stronger olivine-only domains deformed by dislocation creep. All of these experimental studies have PSC $\geqq 4$ and develop S–C′ fabrics, which agrees with our observation that the S–C fabric only occurs at very low PSC where strain is nearly homogeneous.

Shear experiments on monomineralic aggregates also demonstrate the relationship between fabric and PSC. In quartzites deforming by low temperature dislocation creep it is common to observe localization of strain in bands of strain-free recrystallized quartz grains in the C′ orientation at low strain (Fig. 4a) and flattening of the remaining porphyroclasts in the S orientation. The formation of the S–C′ fabric in the monophase aggregates is due to strain partitioning between porphyroclasts that have high dislocation densities and small recrystallized grains along the grain boundaries that are initially dislocation-free (e.g. regime 1 of Hirth and Tullis (1992)). However, with increasing strain or as the percent recrystallized grains increases, removing work hardened porphyroclasts and creating a lower 'phase' strength contrast, there is a change to an S–C fabric (Figs. 4d and 8a). At conditions where dislocation climb is rapid (e.g. regimes 2 and 3 of Hirth and Tullis (1992)), porphyroclasts and recrystallized grains have little strength contrast and form S–C fabrics early in their strain history (Heilbronner and Tullis, 2002). At low strain, regime 2 samples are transitional between the two fabrics (S–C′ or S–C) because slip is easy in porphyroclasts of some orientations, but not in others. At the lowest stresses, i.e. in regime 3, strain is relatively homogeneous among porphyroclasts and recrystallized grains from the initiation of deformation onward. The experimental results also indicate that low strain S–C′ fabrics may be transient and that as the porphyroclasts recrystallize or weaken with strain the fabrics may evolve to an S–C fabric.

These experimental results are similar to the observations of Lister and Snoke (1984), who found that in highly recrystallized natural quartzites (probably deforming by climb-accommodated dislocation creep) the long axes of the quartz grains and the relatively undeformed parts of mica fish were in the S plane and small recrystallized mica grains were located in the C plane. This fabric indicates that at the conditions of deformation of these quartzites there was a low PSC, which is reasonable at mid- to lower-crustal conditions based on the flow laws for muscovite and quartz (Mares and Kronenberg (1993) and Hirth et al. (2001), respectively).

Goodwin and Tikoff (2002) have made similar inferences concerning the development of S–C′ and S–C fabrics in a wide variety of materials undergoing transpressional deformation. They frame their arguments in terms of the kinematics of flow within a polyphase aggregate, focusing on the instantaneous directions of flow (apophyses, essentially vectors) in aggregates of different competency contrast among the constituent phases (similar to PSC). They posit that the orientations of flow apophyses are dependent on whether the thinning component of transpressional deformation is localized or homogeneously distributed. Localized flow produces a flow apophysis in the C′ plane, whereas distributed flow produces a flow apophysis more parallel to the shear (C) plane. They conclude that a high competency contrast between the weak and hard phases causes localization of strain into shear bands (C′) composed of the weak phase. Although they present examples of kinematic evidence for the PSC dependence of fabrics in a variety of materials, they do not develop a criterion for inferring the strength or relative strengths of the weak and strong phases based on the fabric that develops.

Based on the results of our study presented above we believe it is possible to use fabric type to estimate the bulk strengths of polyphase aggregates. The examples of S–C′ fabrics in the literature all have PSC greater than $5\times$ (e.g. Jordan, 1987; Stuenitz and Tullis, 2001; Holtzman et al., 2003), but in our study the lowest PSC that produces a S–C′ fabric is approximately $3\times$ and the S–C fabric is only produced at very low PSC, approaching $1\times$. This observation is important because the lack of strain partitioning in the S–C fabric samples suggests that the strength of polyphase aggregates with S–C fabrics can be approximated by the strength of the dominant (interconnected) phase. Field geologists can directly measure the recrystallized grain size in natural S–C shear zones and determine the flow stress in the shear zone. However, in rocks with S–C′ fabrics the presence of strain localization makes it impossible to approximate the flow stress of the aggregate based on a monophase flow law for one of the constituent phases. Until a realistic model for predicting the strength and its relation to textural evolution in polyphase aggregates is

developed, it is impossible to accurately estimate the true strength of crustal shear zones with a high PSC from the strength of one of the constituent phases.

4.5. Effects of fabric anisotropy and weak phase content

Two additional factors that may affect the strength of polyphase rocks and the development of deformation fabrics are the percentage of weak phase in the protolith and the degree of pre-existing anisotropy (e.g. foliation). Shea and Kronenberg (1993) investigated the influence of both factors for deformation in the brittle field in axial compression experiments on mica-bearing schists and gneisses with varied mica contents (15–75%). Rocks with initially isolated micas ($<$ 25%) in a quartz–feldspar framework were strong and failed brittlely; rocks with initially interconnected micas ($>$25%) were weaker and strain was accommodated within multiple mica-rich zones. Similar results have been reported for experiments on quartz–mica in the ductile regime (Tullis and Wenk, 1994). Thus, when the PSC is high, strain tends to be highly localized when the weak phase is present in smaller amounts and is initially isolated, as in our 800F experiments on Gneiss Minuti. However, strain is more homogeneous when the weak phase is more abundant and initially interconnected; this is the case for our 800S experiments because at these conditions the quartz and biotite are almost equally weak.

The presence of a strong foliation in our Gneiss Minuti samples maximized the PSC between the biotite and the quartz framework, because the biotites were in their weakest orientation, parallel to the shear plane. However, in feldspathic rocks without a foliation, such as granites, the percentage of weak phase is effectively decreased because some of the mica grains are in a strong orientation. Thus, two rocks with the same percentage of mica, but different degrees of foliation, can have different peak strengths. This factor is well demonstrated by the difference in strength observed for similar quartz–feldspar rocks with initially isolated biotite grains, where one was a well-foliated gneiss (Gottschalk et al., 1990) and the other was a granite (Tullis and Yund, 1987). The foliated gneiss, with biotites in their weakest orientation, is 22% weaker than the granite, but the strength of the foliated gneiss is similar to the granite when the biotites are in their strongest orientation. Therefore, if the final flow stress after mica interconnection occurs is the same in granitic rocks with similar mica contents, but different initial starting mica anisotropies/orientations, both the strain weakening and the strain necessary to reach the steady state flow stress will be greater in rocks with initially random orientations of micas or micas in predominantly strong orientations than that in rocks with a previous foliation oriented for easy slip on mica grains.

4.6. Comparison with field studies and application to nature

Rocks with lower PSC deform more homogeneously, and thus in naturally deformed rocks more homogeneous strain is expected at higher temperature or slower strain rate due to the decreasing PSC between a given set of minerals. This tendency is well illustrated by the difference in the degree of strain localization between our 800F and 800S samples. Although biotite in both samples partially dehydrates to form a weak mix of fine-grained biotite, garnet and Fe/Ti oxides, the degree of strain localization is lower in the 800S sample, due to the lower strength of the quartz framework and thus the lower PSC.

The Gneiss Minuti starting material has a quartz framework, but many polyphase rocks in the crust, including granitic rocks, have a feldspar framework, with quartz and mica as the isolated weak phases. The experimental study of Dell'Angelo and Tullis (1996) showed that the same tendency for weak phase (quartz) interconnection occurred with progressive strain, even in the geometrically less favorable case of axial compression.

Several studies have described natural mica-bearing shear zones, with no reaction, in granitic rocks (Voll, 1976; Berthe et al., 1979; Gapais, 1989; Lonka et al., 1998; Johnson et al., 2004; Vernon et al., 2004). In most of these studies the mechanisms that led to the interconnection of the micas are not known, but the microstructures and fabrics are similar to those observed in the high-strain Gneiss Minuti samples of this study (Voll, 1976; Berthe et al., 1979; Gapais, 1989; Lonka et al., 1998). Lonka et al. (1998) described microstructures preserved across a wide strain gradient adjacent to the Suomusjarvi shear zone, which cross-cuts a tonalite in southwestern Finland. A strain gradient exists from relatively undeformed tonalite with an igneous texture and large grain size ($\sim$5 mm) to an ultramylonite with a very fine-grained ($<$10 μm) mixed-phase assemblage of quartz, plagioclase, and biotite containing only 10–30% small clasts. In the least deformed zones biotite and quartz are weak relative to the plagioclase, and are localized into shear bands forming an S–C′ fabric. With progressive strain (closer to the ultramylonite zone), plagioclase grains are more recrystallized, and the fine-grained quartz, biotite, and plagioclase begin to mix, forming a mixed-phase aggregate which partitions strain. The mechanisms for interconnection of the mica and quartz are not described in this paper, but most likely stress concentrations in plagioclase grains adjacent to isolated quartz grains or to tips of biotite grains led to local cataclasis, and these fine grains subsequently recrystallized (e.g. Stuenitz et al., 2003).

Studies of a strain gradient within the margins of a tonalitic pluton by Vernon et al. (2004) and Johnson et al. (2004) are unusual because some evidence of the biotite interconnection mechanism is preserved, although they are also complex because melt was probably present during the early stages of deformation. Low strain samples preserve evidence for local brittle deformation of feldspars adjacent to biotite grains, and resulting biotite interconnection. The presence of melt somewhat confuses the interpretation due to the possibility of pore pressure embrittlement (e.g. Davidson et al., 1994). Whatever the cause of the local brittle deformation, the resulting interconnection of the initially dispersed biotite grains caused subsequent strain to be strongly partitioned. Johnson et al. (2004) modeled the deformation as entirely solid state, and calculated that the stresses adjacent to weak biotite grains in a plagioclase matrix were twice the confining pressure of 300 MPa. Once the biotite grains became linked the calculated

strain rate in the biotite-rich zones was two orders of magnitude higher than that in the plagioclase.

The results of our study also agree with direct measurements of strain partitioning in other natural polyphase meso- and mega-scale shear zones by Keller et al. (2004) and Norris and Cooper (2003). The similarity of the results at all scales indicates that the phase strength contrast between different units/lithologies controls the structures produced during deformation of larger regions and that the same stress-concentration induced variation in deformation mechanisms within individual lithologies may lead to formation of these large-scale shear zones.

5. Conclusions

A series of shear experiments was performed on a fine-grained biotite + plagioclase + quartz gneiss; the quartz (58%) forms an interconnected framework and the biotite (13%) is aligned but not interconnected. The experiments were performed at 1500 MPa, and three temperature/strain rate combinations (800 °C/$\sim 10^{-5}$ s^{-1}, 745 °C/$\sim 10^{-6}$ s^{-1}, and 800 °C/$\sim 10^{-6}$ s^{-1}) that produced three different initial phase strength contrasts (45×, 25×, and 10×). Samples were sheared to a range of different strains to determine the evolution of deformation mechanisms and fabrics as the weak biotites became interconnected and the rheology was no longer controlled by a load-bearing framework but by an interconnected weak phase. Samples deformed at the highest PSC (45×) conditions developed a single highly localized shear zone. The samples deformed at an intermediate PSC (25×) did not develop a localized shear zone although strain was partitioned into multiple zones of interconnected biotites and recrystallized quartz grains, producing a penetrative S–C′ fabric. Samples deformed at the lowest PSC (~10×) initially developed an S–C′ fabric, but it evolved to an S–C fabric as the quartz weakened and the PSC was reduced, allowing the quartz and interconnected biotite zones to deform homogeneously. After shear zone formation in the highest PSC sample quartz microstructures indicate that the strain rate within the shear zone was an order of magnitude faster than the imposed strain rate, and that in the host rock was an order of magnitude slower. In contrast, quartz microstructures observed in the lowest PSC samples were homogeneous throughout each sample, although they evolved with strain.

Some general conclusions include:

(1) The strain-induced interconnection of weak phases in a strong framework is an important cause of ductile strain localization and weakening.
(2) Stress concentrations in stronger framework grains surrounding the weak phase can produce a heterogeneous distribution of deformation mechanisms in the framework and enhance the local failure of the framework grains.
(3) The grain-scale deformation mechanisms which initiate ductile shear zones are not the ones that dominate after deformation is localized, due to changes in flow stress and in local strain rates.
(4) The degree of strain localization decreases with a decrease in the strength contrast between weak and strong phases, resulting in different fabrics: S–C′ fabrics form at higher PSC and S–C fabrics form at low PSC.

Acknowledgements

This work was supported by an NSF grant to JT (EAR-0208150). CH and JT would like to thank Bill Collins for preparing the many TEM sections necessary for this study, Michael Stipp for discussions and performing CIP analyses on sample W-1020, Dick Yund, Peter Gromet, Laurel Goodwin, Basil Tikoff and Holger Stunitz for stimulating discussions, and Chris Spiers and Stephen Covey-Crump for thorough and thought-provoking reviews. CH would like to especially thank Mark Handy, Michele Zucali and Giulio DiToro for assistance in obtaining the Gneiss Minuti starting material and Andy Kronenberg, whose low temperature studies on the deformation of mica-bearing rocks with various collaborators in the early 1990s initially inspired this study.

References

Berthe, D., Choukroune, P., Jegouzo, P., 1979. Orthogneiss, mylonite and non coaxial deformation of granites; the example of South Armorican shear zone. Journal of Structural Geology 1 (1), 31–42.

Bons, P.D., Cox, S.J.D., 1994. Analogue experiments and numerical modelling on the relation between microgeometry and flow properties of polyphase materials. Materials Science and Engineering. A, Structural Materials: Properties, Microstructure and Processing 175 (1–2), 237–245.

Bos, B., Spiers, C.J., 2001. Experimental investigation into the microstructural and mechanical evolution of phyllosilicate-bearing fault rock under conditions favouring pressure solution. Journal of Structural Geology 23 (8), 1187–1202.

Bos, B., Spiers, C.J., 2002. Frictional-viscous flow of phyllosilicate-bearing fault rock; microphysical model and implications for crustal strength profiles. Journal of Geophysical Research 107 (B2), 2028. doi:10.1029/2001JB000301.

Davidson, C., Schmid, S.M., Hollister, L.S., 1994. Role of melt during deformation in the deep crust. Terra Nova 6 (2), 133–142.

Dell'Angelo, L.N., Tullis, J., 1996. Textural and mechanical evolution with progressive strain in experimentally deformed aplite. Tectonophysics 256 (1–4), 57–82.

Fortier, S.M., Giletti, B.J., 1991. Volume self-diffusion of oxygen in biotite, muscovite, and phlogopite micas. Geochimica et Cosmochimica Acta 55 (5), 1319–1330.

Gapais, D., 1989. Shear structures within deformed granites; mechanical and thermal indicators. Geology 17 (12), 1144–1147.

Gleason, G.C., Tullis, J., 1995. A flow law for dislocation creep of quartz aggregates determined with the molten salt cell. Tectonophysics 247 (1–4), 1–23.

Goodwin, L.B., Tikoff, B., 2002. Competency contrast, kinematics, and the development of foliations and lineations in the crust. Journal of Structural Geology 24 (6–7), 1065–1085.

Gottschalk, R.R., Kronenberg, A.K., Russell, J.E., Handin, J., 1990. Mechanical anisotropy of gneiss; failure criterion and textural sources of directional behavior. Journal of Geophysical Research 95 (13), 21,613–21,634.

Handy, M.R., 1990. The solid-state flow of polymineralic rocks. Journal of Geophysical Research 95 (6), 8647–8661.

Handy, M.R., 1994. Flow laws for rocks containing two non-linear viscous phases; a phenomenological approach. Journal of Structural Geology 16 (3), 287–301.

Heilbronner, R., Tullis, J., 2002. The effect of static annealing on microstructures and crystallographic preferred orientations of quartzites experimentally deformed in axial compression and shear. In: de Meer, S., Drury Martyn, R., de Bresser, J.H.P., Pennock Gill, M. (Eds.), Deformation Mechanisms, Rheology and Tectonics; Current Status and Future Perspectives. Geological Society of London, London, UK, pp. 191–218.

Heilbronner, R., Tullis, J., submitted. Evolution of c-axis pole figures and grain size during progressive grain boundary migration recrystallization: results from experimentally shear quartzite. Journal of Geophysical Research.

Hirth, G., Tullis, J., 1992. Dislocation creep regimes in quartz aggregates. Journal of Structural Geology 14 (2), 145–159.

Hirth, G., Tullis, J., 1994. The brittle–plastic transition in experimentally deformed quartz aggregates. Journal of Geophysical Research 99 (6), 11,731–11,748.

Hirth, G., Teyssier, C., Dunlap, W.J., 2001. An evaluation of quartzite flow laws based on comparisons between experimentally and naturally deformed rocks. International Journal of Earth Sciences 90 (1), 77–87.

Holtzman, B.K., Groebner, N.J., Zimmerman, M.E., Ginsberg, S.B., Kohlstedt, D.L., 2003. Stress-driven melt segregation in partially molten rocks. Geochemistry, Geophysics, Geosystems 4 (5), 1–26.

Holyoke, C.W. III, 2005. Strain weakening in crustal and upper mantle lithologies: processes and consequences. Unpublished Ph.D. thesis, Brown University.

Holyoke, C.W. III, Tullis, J., submitted. The interaction between reaction and deformation: an experimental study using a biotite + plagioclase + quartz gneiss. Journal of Metamorphic Geology.

Imber, J., Holdsworth, R.E., Butler, C.A., Strachan, R.A., 2001. A reappraisal of the Sibson–Scholz fault zone model; the nature of the frictional to viscous ("brittle–ductile") transition along a long-lived, crustal-scale fault, Outer Hebrides, Scotland. Tectonics 20 (5), 601–624.

Johnson, S., Vernon, R., Upton, P., 2004. Foliation development and progressive strain-rate partitioning in the crystallizing carapace of a tonalite pluton: microstructural evidence and numerical modeling. Journal of Structural Geology 26 (10), 1845–1865.

Jordan, P.G., 1987. The deformational behaviour of bimineralic limestone–halite aggregates. Tectonophysics 135, 185–197.

Keller, L.M., Abart, R., Stuenitz, H., De, C.C., 2004. Deformation, mass transfer and mineral reactions in an eclogite facies shear zone in a polymetamorphic metapelite (Monte Rosa Nappe, Western Alps). Journal of Metamorphic Geology 22 (2), 97–118.

Kronenberg, A.K., Kirby, S.H., Pinkston, J., 1990. Basal slip and mechanical anisotropy of biotite. Journal of Geophysical Research 95 (12), 19,257–19,278.

Lister, G.S., Snoke, A.W., 1984. S–C mylonites. Journal of Structural Geology 6 (6), 617–638.

Lonka, H., Schulmann, K., Venera, Z., 1998. Ductile deformation of tonalite in the Suomusjarvi shear zone, south-western Finland. Journal of Structural Geology 20 (6), 783–798.

Mares, V.M., Kronenberg, A.K., 1993. Experimental deformation of muscovite. Journal of Structural Geology 15 (9–10), 1061–1075.

Niemeijer, A.R., Spiers, C.J., 2005. Influence of phyllosilicates on fault strength in the brittle-ductile transition: insights from rock analogue experiments. In: High-Strain Zones: Structure and Physical Properties (edited by Bruhn, D. & Burlini, L.) 245. Geological Society of London, London, 303–327.

Norris, R.J., Cooper, A.F., 2003. Very high strains recorded in mylonites along the Alpine Fault, New Zealand; implications for the deep structure of plate boundary faults. Journal of Structural Geology 25 (12), 2141–2157.

Passchier, C.W., Trouw, R.A.J., 1995. Microtectonics. Springer-Verlag, Berlin.

Poirier, J.P., 1980. Shear localization and shear instability in materials in the ductile field. Journal of Structural Geology 2 (1–2), 135–142.

Post, A., Tullis, J., 1999. A recrystallized grain size piezometer for experimentally deformed feldspar aggregates. Tectonophysics 303 (1–4), 159–173.

Rawling, G., Baud, P., Wong, T., 2002. Dilatancy, brittle strength and anisotropy of foliated rocks: experimental deformation and micromechanical modeling. Journal of Geophysical Research 107 (B10), 2234–2248.

Shea, W.T., Kronenberg, A.K., 1992. Rheology and deformation mechanisms of an isotropic mica schist. Journal of Geophysical Research 97 (11), 15,201–15,237.

Shea, W.T., Kronenberg, A.K., 1993. Strength and anisotropy of foliated rocks with varied mica contents. Journal of Structural Geology 15 (9–10), 1097–1121.

Stewart, M., Holdsworth, R.E., Strachan, R.A., 2000. Deformation processes and weakening mechanisms within the frictional–viscous transition zone of major crustal-scale faults; insights from the Great Glen fault zone, Scotland. Journal of Structural Geology 22 (5), 543–560.

Stipp, M., Tullis, J., 2003. The recrystallized grain size piezometer for quartz. Geophysical Research Letters 30 (21), 2088–2091.

Stipp, M., Stuenitz, H., Heilbronner, R., Schmid, S.M., 2002a. Dynamic recrystallization of quartz; correlation between natural and experimental conditions. In: de Meer, S., Drury Martyn, R., de Bresser, J.H.P., Pennock Gill, M. (Eds.), Deformation Mechanisms, Rheology and Tectonics; Current Status and Future Perspectives. Geological Society of London, London, UK, pp. 171–190.

Stipp, M., Stuenitz, H., Heilbronner, R., Schmid, S.M., 2002b. The eastern Tonale fault zone; a "natural laboratory" for crystal plastic deformation of quartz over a temperature range from 250 to 700 °C. Journal of Structural Geology 24 (12), 1861–1884.

Stuenitz, H., Tullis, J., 2001. Weakening and strain localization produced by syn-deformational reaction of plagioclase. International Journal of Earth Sciences 90 (1), 136–148.

Stuenitz, H., Fitz Gerald, J.D., Tullis, J., 2003. Dislocation generation, slip systems, and dynamic recrystallization in experimentally deformed plagioclase single crystals. Tectonophysics 372, 215–233.

Tullis, J., 2002. Deformation of granitic rocks; experimental studies and natural examples. In: Karato, S.-I., Wenk, H.R. (Eds.), Plastic Deformation of Minerals and Rocks. Mineralogical Society of America and Geochemical Society, Washington, DC, USA, pp. 51–95.

Tullis, J., Wenk, H.R., 1994. Effect of muscovite on the strength and lattice preferred orientation of experimentally deformed quartz aggregates. Materials Science and Engineering. A, Structural Materials: Properties, Microstructure and Processing 175 (1–2), 209–220.

Tullis, J., Yund, R.A., 1987. Transition from cataclastic flow to dislocation creep of feldspar; mechanisms and microstructures. Geology 15 (7), 606–609.

Tullis, J., Yund, R., 1992. The brittle–ductile transition in feldspar aggregates; an experimental study. In: Evans, B., Wong, T.F. (Eds.), Fault Mechanics and Transport Properties of Rocks; a Festschrift in Honor of W.F. Brace. Academic Press, San Diego, CA, USA, pp. 89–117.

Tullis, T.E., Tullis, J., 1986. Experimental rock deformation techniques. In: Mineral and Rock Deformation; Laboratory Studies; The Paterson Volume 36. American Geophysical Union, Washington, DC, USA, pp. 297–324.

Vernon, R., Johnson, S., Melis, E., 2004. Emplacement-related microstructures in the margin of a deformed tonalite pluton: the San Jose tonalite, Baja California, Mexico. Journal of Structural Geology 26, 1867–1887.

Voll, G., 1976. Recrystallization of quartz, biotite and feldspars from Erstfeld to the Leventina Nappe, Swiss Alps, and its geological significance. Schweizer Mineralogische und Petrographische Mitteilungen 56, 641–647.

White, S.H., Burrows, S.E., Carreras, J., Shaw, N.D., Humphreys, F.J., 1980. On mylonites in ductile shear zones. Journal of Structural Geology 2 (1–2), 175–187.

Zurbriggen, R., Kamber, B.S., Handy, M.R., Naegler, T.F., 1998. Dating synmagmatic folds; a case study of Schlingen structures in the Strona–Ceneri Zone (Southern Alps, northern Italy). Journal of Metamorphic Geology 16 (3), 403–414.